

Modeling Globular Cluster Stellar Streams with a Basis-Expansion N -body Code

BRIAN T. COOK ,¹ KERWANN TEP ,² CARL L. RODRIGUEZ ,¹ LEAH ENGLISH,³ TJITSKE STARKENBURG ,^{4,5,6}
 ROBYN SANDERSON ,⁷ NEWLIN C. WEATHERFORD ,⁸ SARAH PEARSON ,⁹ AND NONDH PANITHANPAISAL ,^{8,10}

¹Department of Physics and Astronomy, University of North Carolina at Chapel Hill, 120 E. Cameron Ave, Chapel Hill, NC, 27514, USA

²Observatoire Astronomique de Strasbourg, UMR 7550, 11 rue de l'Université, Strasbourg 67000, France

³Department of Physics, Illinois Institute of Technology, 3105 S Dearborn St, Chicago, IL, 60616, USA

⁴Department of Physics and Astronomy, Northwestern University, 2145 Sheridan Rd, Evanston IL 60208, USA

⁵Center for Interdisciplinary Exploration and Research in Astrophysics (CIERA), Northwestern University, 1800 Sherman Ave, Evanston IL 60201, USA

⁶NSF-Simons AI Institute for the Sky (SkAI), 172 E. Chestnut St., Chicago, IL 60611, USA

⁷Department of Physics & Astronomy, University of Pennsylvania, 209 S 33rd St, Philadelphia, PA 19104, USA

⁸Observatories of the Carnegie Institution for Science, 813 Santa Barbara St, Pasadena, CA 91101, USA

⁹DARK, Niels Bohr Institute, University of Copenhagen, Jagtvej 155A, 2200 Copenhagen, Denmark

¹⁰TAPIR, Mailcode 350-17, California Institute of Technology, Pasadena, CA 91125, USA

ABSTRACT

Globular cluster stellar streams probe galaxy-formation processes and can potentially reveal the distribution of dark matter in galaxies. In many theoretical studies, streams are modeled with particle-spray or direct N -body codes. But particle-spray methods abstract away the internal dynamics of the progenitor by making strong assumptions about the escape physics, while direct N -body is prohibitively expensive for realistic ($N > 10^5$) systems. In this paper, we present the stream-modeling capabilities of KRIOS, a new basis-expansion N -body code for collisional stellar dynamics, that bridges this runtime vs. accuracy gap. We show that KRIOS reproduces NBODY6++GPU cluster models, and their associated streams, more accurately than particle spray in a fraction of the NBODY6++GPU wall-clock time. We then compare KRIOS to various particle-spray methods on 10 orbits similar to known Milky Way streams. The morphology and kinematics of these streams most disagree when the progenitor is tightly bound to the host, as these systems are often subject to stronger tidal forces. Finally, we discuss which elements of the progenitor physics are most important for modeling stellar streams and how these might be incorporated into particle-spray methods.

Keywords: N -body simulations (1083) – Globular star clusters (656) – Stellar streams (2166)

1. INTRODUCTION

There are lingering discrepancies between Local-Group-scale Λ CDM predictions and observations (Bullock & Boylan-Kolchin 2017) that near-field cosmologists are eager to rectify. The Milky Way (MW) and its population of globular clusters (GCs) could provide key insight into these tensions. GCs can either form *in situ* as a mode of star formation in galaxies, or can be accreted from other galaxies during mergers (Katz & Ricotti 2013; Belokurov & Kravtsov 2024). Both formation channels can help constrain the MW's formation history (e.g., Katz & Ricotti 2013; Kruijssen et al. 2020; Malhan et al. 2022; Chen & Gnedin 2024). Conversely, the

host environment of the MW plays a key role in the dynamical evolution of its GCs. As the Galactic potential changes along a cluster's orbit, the loss of stars to the tidal field can significantly accelerate the destruction of Galactic GCs (e.g., Gnedin & Ostriker 1997). These lost stars go on to create debris such as stellar streams (e.g., Lynden-Bell & Lynden-Bell 1995) or shells (e.g., Peñarrubia et al. 2009), which probe the Galactic potential. Accurate, long-term models of GC evolution that include interactions with their host galaxy (e.g., Riley & Strigari 2020) would thus improve both galaxy-formation (e.g., Cole et al. 2000; Bullock & Johnston 2005) and GC studies.

The dynamically cold streams from GCs, in particular, are highly sensitive to perturbations from substructure within the host galaxy (see Bonaca & Price-Whelan 2025, for a review), including both baryonic substructure (e.g., Pearson

Corresponding author: Brian T. Cook
 btcook@unc.edu

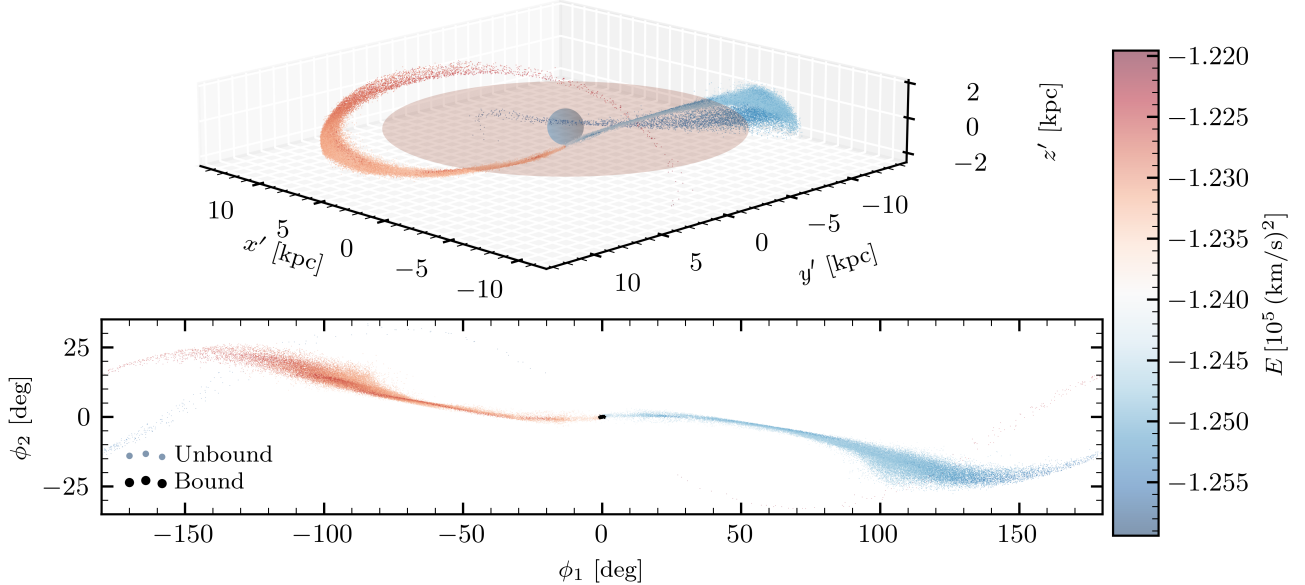


Figure 1. A model produced by the KRIOS hybrid N -body code (Orbit 3, Table 1), where we see both stream-like and shell-like features at $t=5$ Gyr. The unbound particles are color coded by their energy with respect to the host E , which is mostly conserved for escapers modulo small perturbations from the cluster potential. The bound particles (Section 2.2) are shown in black. *Top panel:* The stream shown in the MW’s reference frame, with a bulge and disk added for illustrative purposes. *Bottom panel:* The stream shown in the great-circle reference frame for an observer stationed at the Galactic center. The angle ϕ_1 subtends an element of the stream track and ϕ_2 subtends the angle out of the progenitor’s instantaneous orbital plane (see Figure 2 for the axis definitions). The stream progenitor (i.e., the cluster) is at $\phi_1=\phi_2=0^\circ$. Both the leading (blue) and trailing (red) tails contain epicyclic density fluctuations (Küpper et al. 2010) and energy feathering (Amorisco 2015), both well-known features of streams in axisymmetric potentials (Bonaca & Price-Whelan 2025). The density fluctuations are most clear near the progenitor; see Figure 9 for a direct comparison.

et al. 2017; Amorisco 2017) and dark matter subhalos (e.g., Yoon et al. 2011; Carlberg 2012; Erkal et al. 2016). The presence of dark subhalos, which are clumps of dark matter too small to form stars, in galaxies is a key prediction of Λ CDM and a potential clue to the nature of dark matter itself (e.g. Spergel & Steinhardt 2000; Bullock & Boylan-Kolchin 2017). Several GC streams in the MW, including the GD-1 stream (Grillmair & Dionatos 2006), display features that may have been the result of an encounter with a subhalo (e.g., Bonaca et al. 2019). The kinematic temperature of GC streams is also thought to depend on the subhalo mass-concentration relation (Peñarrubia et al. 2006; Bovy et al. 2017; Carlberg 2025). However, substructure in GC streams can also be the result of the GC progenitor’s properties and internal evolution (e.g., Weatherford & Bonaca 2025), interactions with baryonic substructure in the host galaxy, or larger perturbations in the host potential itself (e.g., Weerasooriya et al. 2025; Guillaume et al. 2026). Distinguishing which features of a stream are caused by its progenitor from those caused by the baryonic or DM substructure of the host galaxy is crucial to successfully probing dark matter physics with stellar streams.

The first approach for modeling dense GCs is often a direct N -body integration, where the forces between pairs of

stars are directly summed every timestep. The gold standard for this is the NBODY6++GPU code (Aarseth 1999; Wang et al. 2015). A variation of the same code allows the GC to be coupled to an external tidal field as well (nbody6tt, Renaud & Gieles 2015), following both the progenitor and resultant stream self-consistently within a time-independent host potential. But the direct summation of forces required to solve N coupled ordinary differential equations (ODEs) requires $\mathcal{O}(N^2)$ operations, making this technique computationally expensive. Despite significant algorithmic enhancements (e.g., regularization of close encounters and block timesteps) and hardware acceleration (e.g., GPUs), direct summation still has not been used to model a GC with a density and initial N typical of Galactic GCs over a full Hubble time. Direct N -body methods are thus ill-suited to generating the large grids of model streams necessary to explore the dynamics within and external to GCs that affect stream properties relevant to probing Galactic substructure.

To hasten computation, stream models rely on more approximate methods. Particle-spray codes (e.g., Küpper et al. 2012; Gibbons et al. 2014; Fardal et al. 2015; Erkal et al. 2019; Grondin et al. 2022; Chen et al. 2025c; Palau et al. 2025) generate stream models far more rapidly than direct N -body by approximating the escape process, directly in-

jecting stars near the Lagrange points of the GCs as they orbit their host. For example, (Fardal et al. 2015, hereafter Fardal15) and (Chen et al. 2025c, hereafter Chen25) sample the rate and kinematic properties of escaping stars from distributions tuned to mimic N -body simulations of tidal disruption (Dehnen 2000; Stadel 2001; Dehnen 2002). While these methods excel in generating large ensembles of models, they assume that the details of the tidal-stripping process do not substantially affect stream properties such as its density and velocity dispersion profiles. Furthermore, most particle-spray studies in the literature have assumed a fixed progenitor (Grondin et al. 2022; Kuzma et al. 2025) or no progenitor at all (otherwise known as orbit fitting, e.g., Koposov et al. 2010; Malhan & Ibata 2019), both of which limit their ability to resolve realistic stream production over long timescales where the cluster has a time-dependent size and mass.

What is needed is an approach that can accurately model an evolving, collisional GC and its ejecta in a fraction of the direct N -body wall-clock time. In numerical studies of GCs, this is often done with Monte Carlo methods, where the collisional evolution of dense star clusters can be approximated by statistical techniques. Leading codes in this area include MOCCA (Giersz et al. 2013) and CMC (Rodriguez et al. 2022), both of which use the Hénon (1971) method to approximate two-body relaxation (Spitzer 1987) via effective “super-encounters” with a nearby neighbor. The Hénon method scales as $\mathcal{O}(N \log N)$, satisfying the need for star-by-star GC simulations with $\mathcal{O}(< N^2)$ complexity that can capture the cluster’s gravothermal evolution and conserve the integrals of motion. As an example, Rodriguez et al. (2016) showed that CMC produces models with $N=10^6$ that agree with NBODY6++GPU on important structural and stellar population properties in about a day; by comparison, the same cluster model integrated with NBODY6++GPU required approximately six months of wall-clock time (Wang et al. 2016).

However, Hénon-style Monte Carlo codes like CMC assume that the cluster is spherically symmetric, with all the relevant dynamical processes occurring on a relaxation timescale (Rodriguez et al. 2022). In reality, the tidal force is anisotropic in the cluster reference frame and can do work on the cluster on a dynamical timescale. Stars ejected at low energies can only escape through openings in the zero-velocity surface near the L_1/L_2 Lagrange points, even after the star has become energetically unbound from the system. As such, it typically requires many dynamical times for a star to actually exit the cluster (Fukushige & Heggie 2000; Weatherford et al. 2024). To account for this, most Monte Carlo codes adopt prescriptions that approximate the tidal radius of the cluster (e.g., Giersz et al. 2008; Chatterjee et al. 2010) and introduce delays to the stripping of particles from the sys-

tem (e.g., Giersz et al. 2013; Sollima & Mastrobuono Battisti 2014). These prescriptions must be tuned to direct N -body simulations of clusters on specific orbits, and are not necessarily reliable for other orbits in a different, or time-varying, host potential. Furthermore, because escapers have to be removed from CMC and its spherical collisional dynamics before evolving their orbits (collisionlessly) in a realistic asymmetric tidal field, these Monte Carlo methods require significant post-processing to model tidal debris in a Galactic context (e.g., Weatherford et al. 2024; Weatherford & Bonaca 2025; Panithanpaisal et al. 2025).

This combination of requirements has motivated the development of KRIOS, a new N -body code introduced by (Tep et al. 2025, hereafter Paper I). Figure 1 provides an illustrative KRIOS model of a GC stellar stream in a MW-like host potential. KRIOS integrates each particle in a self-consistent gravitational field (SCF; Clutton-Brock 1973; Hernquist & Ostriker 1992; Zhao 1996; Lowing et al. 2011; Vasiliev 2015; Fouvry et al. 2021) that adapts as the cluster evolves (Paper I), while two-body relaxation is modeled using a 3D version of Hénon’s original effective encounters. The force calculations are $\mathcal{O}(N)$ and parallelizable, rendering complete forward models considerably faster than direct N -body methods. KRIOS replicates key dynamical properties of non-rotating clusters (such as core collapse in clusters with varying levels of initial velocity anisotropy), as well as rotating clusters (such as the collisional evolution of a cluster’s rotation curve, and the emergence of the radial orbit instability in highly anisotropic clusters). See Paper I for details. Because KRIOS integrates the stellar orbits in a non-spherical cluster on a dynamical timescale, it is well suited to exploring the production of tidal debris from disrupting star clusters in a fraction of the direct N -body wall-clock time.

In Section 2, we introduce the scaffolding that helps KRIOS resolve mass loss due to external tidal fields. In Section 3, we show comparisons between the streams produced by KRIOS and NBODY6++GPU to validate our method, as well as comparisons to various particle-spray methods, in order to explore the regions of Galactic orbital space where the reliability of the latter breaks down. The discussion (Section 4) highlights the benefits of using KRIOS design elements in modeling stellar streams, and describes key features relevant to future particle-spray studies

2. METHODS

KRIOS decomposes the gravitational interactions in a star cluster into collisionless and collisional components. The collisionless gravitational potential is modeled by expanding

the cluster's mass density with a set of basis functions:

$$\psi_{\text{SCF}}(\mathbf{r}) = \sum_{n\ell m} a_{n\ell m} \psi^{(n\ell m)}(\mathbf{r}), \quad (1a)$$

$$\rho_{\text{SCF}}(\mathbf{r}) = \sum_{n\ell m} a_{n\ell m} \rho^{(n\ell m)}(\mathbf{r}). \quad (1b)$$

The basis functions are separable in spherical coordinates:

$$\psi^{(n\ell m)}(\mathbf{r}) = U_n^\ell(r) Y_\ell^m(\theta, \phi), \quad (2a)$$

$$\rho^{(n\ell m)}(\mathbf{r}) = D_n^\ell(r) Y_\ell^m(\theta, \phi), \quad (2b)$$

where n, ℓ index the radial basis functions $\{U_n^\ell(r), D_n^\ell(r)\}$ and ℓ, m index the spherical harmonics $Y_\ell^m(\theta, \phi)$. In the standard self-consistent field approach, $\psi^{(n\ell m)}$ and $\rho^{(n\ell m)}$ are bi-orthogonal sets where each mode constitutes an independent solution to Poisson's equation such that $\nabla^2 \psi^{(n\ell m)} = 4\pi G \rho^{(n\ell m)}$. The bi-orthogonality relation can be used to isolate each basis coefficient $a_{n\ell m}$:

$$a_{n\ell m} = - \int d\mathbf{r} \rho(\mathbf{r}) \psi^{*(n\ell m)}(\mathbf{r}), \quad (3a)$$

$$\simeq - \sum_k m_k \psi^{*(n\ell m)}(\mathbf{r}_k), \quad (3b)$$

where $\psi^{(n\ell m)*}$ is the complex conjugate of $\psi^{(n\ell m)}$ and we have estimated the cluster's mass density from the particle data as $\rho(\mathbf{r}) \simeq \sum_k m_k \delta^3(\mathbf{r} - \mathbf{r}_k)$.

The individual stars are then integrated forward in the global $\psi_{\text{SCF}}(\mathbf{r})$ potential. This reduces the N^2 calculation of direct N -body to N individual, embarrassingly parallel integrations. In general, the greatest computational bottleneck for the SCF method is the large number of modes that are required when the basis functions are not well fit to the cluster's mass density (Hernquist & Ostriker 1992). To address this, KRIOS uses a tunable set of basis functions from Zhao (1996), where the zeroth-order mode of the potential has the following functional form:

$$U_0^0(r) \propto \frac{1}{\left(1 + \left(\frac{r}{b}\right)^{1/\alpha}\right)^\alpha}, \quad (4)$$

(Appendix A of Paper I). KRIOS tunes the exponent α and scale length b such that the true cluster potential is well approximated by the zeroth-order mode of the SCF even as the density profile becomes cuspy near core collapse (Figure 9 of Paper I). This, combined with a filtering procedure that ignores modes where $a_{n\ell m} \ll a_{000}$, allows KRIOS to maintain an optimized description of the cluster potential over many relaxation times. See Section 2.2 of Paper I for details.

Finally, KRIOS models the relaxation of star clusters with the Hénon (1971) prescription, where the cumulative effect

of many two-body encounters are modeled as a single effective “super-encounter” between a star and a suitably chosen neighbor. We approximate the local number density of particles, a key ingredient for computing the relaxation timescale (Section 2.1.1 of Rodriguez et al. 2022), using $n_{\text{neigh}} = 30$ neighbors. We then update each particle's 3D velocity based on the relevant two-body super-encounter at each system timestep. These scattering events diffuse energy from the cluster's core to its halo, and have been shown to reproduce the expected gravothermal evolution and core collapse of star clusters over many relaxation times; see Paper I. Note that we do not apply the energy conservation scheme from Stodolkiewicz (1982) in this study. This scheme is often used to correct the energy drift observed in Monte Carlo codes (e.g., Rodriguez et al. 2022) that arises from sampling new orbital positions and velocities (post two-body relaxation) in the old cluster potential from the previous timestep. In this study, however, the cluster potential is updated much more frequently (see Section 2.2). As a result, our models conserve energy in the host frame of the Galaxy E ($\Delta E/E_0 \lesssim 10^{-3}$) and the z' component of the angular momentum $L_{z'}$ ($\Delta L_{z'}/L_{z',0} \lesssim 10^{-2}$) at acceptable levels over the 5 Gyr integrations presented here.

2.1. KRIOS Reference Frames

KRIOS uses accelerating, non-rotating reference frames for the SCF, which mitigates the need to include rotational pseudo-forces into the equations of motion explicitly (Renaud et al. 2011). Our framework is illustrated in Figure 2. For a static host potential, we set the fixed inertial frame to coincide with the center of the bulge, disk, and dark matter halo components (the primed coordinates in Figure 2).

KRIOS has separate reference frames for the host potential and the cluster. The position of the cluster frame (unprimed coordinates, Figure 2) is set to the location that maximizes the a_{000} component of the basis expansion (using a similar procedure for finding the optimal α and b in Equation (4)). Because the SCF basis does not contain any information about the velocity of the system, the velocity for the reference frame is determined by taking a mass-weighted average of the particle velocities in the cluster's core, where $r_{\text{core}} = \sqrt{\sum_i \rho_{\text{SCF}}^2(\mathbf{r}_i) r_i^2 / \sum_i \rho_{\text{SCF}}^2(\mathbf{r}_i)}$.¹

In order to return accurate solutions to each particle's equations of motion, the ODE solver must be able to determine each particle's location with respect to both the SCF and host at arbitrary times during each integration (purple segments in Figure 2). As such, each star must have access to the position of the cluster at arbitrary times along its orbit. To that

¹ This is similar to the definition used in traditional N -body integrators (Paper I) where we substitute the computationally expensive calculation of the full particle density with the mass density of the SCF.

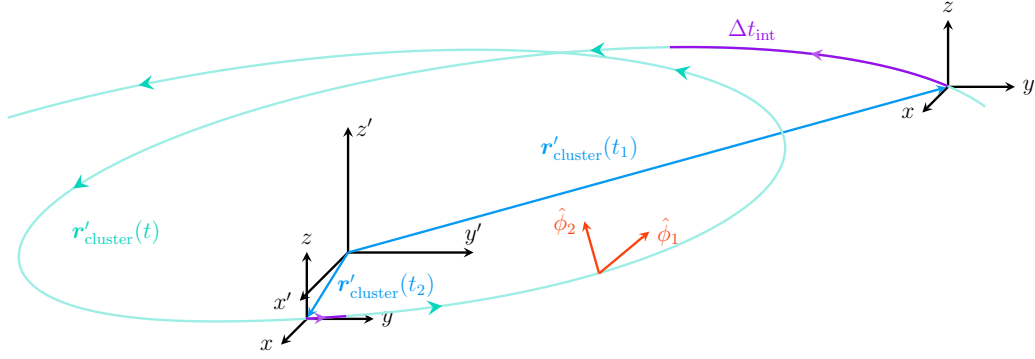


Figure 2. The time-dependent SCF reference frame (black, unprimed) with respect to the fixed host reference frame (black, primed). Integration along the orbit (green) is broken up into substeps (purple) that adapt to the host potential’s tidal tensor (Equation (6)). The unit vectors that define the great-circle reference frame (bottom panel of Figure 1, red axes) are $\hat{\phi}_1 \parallel (\Omega'_{\text{cluster}} \times \mathbf{r}'_{\text{cluster}})$ and $\hat{\phi}_2 \parallel \Omega'_{\text{cluster}}$, where $\Omega'_{\text{cluster}} \parallel \mathbf{r}'_{\text{cluster}} \times \mathbf{v}'_{\text{cluster}}$.

end, we integrate a test particle—located at the cluster’s center of mass²—in the host potential, and collect position and velocity samples along that orbit. These samples are then used to create a quintic Hermite spline (Finn 2004; Rehman 2014), to determine the position of the cluster at arbitrary times. Each star can then be integrated forward in the host reference frame individually, without the need to synchronize the center of the cluster after every individual particle integration step.

2.2. Cluster Timescales in an External Potential

For the collisional models in Paper I, the KRIOS system timestep was chosen to be a fraction of the relaxation time of the cluster. After the particles were integrated forward in the potential, we performed two-body relaxation and updated the SCF potential using the new positions of the particles, on the assumption that the potential of the cluster could only change significantly on a relaxation timescale. However, for clusters in realistic tidal fields, the associated mass loss can occur faster than the typical relaxation timescale in the core. Furthermore, the external potential of the host can do work on the cluster on a dynamical timescale, e.g. compressive shocks from the Galactic disk (Section 5.2.a of Spitzer 1987) and during perigalacticon passages like $\mathbf{r}'_{\text{cluster}}(t_2)$ in Figure 2. To resolve this, we introduce separate timesteps for performing two-body relaxation and updating the cluster potential:

- The **system timestep**, Δt_{sys} , where we perform two-body relaxation and completely recompute the cluster SCF, as in Equation (14) of Paper I.

² There is typically a small difference between the cluster’s center of mass and the optimal location for the SCF; we assume that separation vector, $\Delta \mathbf{r}' \equiv \mathbf{r}'_{\text{COM}} - \mathbf{r}'_{\text{SCF}}$, to be constant during each integration.

- The **integration timestep**, Δt_{int} , where we update the SCF potential on a timescale set by the changing tidal field experienced by the cluster.

To calculate Δt_{int} , we evaluate the tidal tensor (\mathbf{T} , the Hessian of the potential) at every point along the orbit of the cluster test particle described in Section 2.1. Following Grudić & Hopkins (2020), we define the integration timestep as

$$\Delta t_{\text{int}} = \sqrt{\eta} \left(\frac{1}{6} \|\mathbf{T}(\mathbf{r}'(t))\|^2 \right)^{-1/4}, \quad (5)$$

where $\|\cdot\|$ is the Frobenius norm of the tidal tensor, computed with respect to the primed coordinates,

$$T_{ij}(\mathbf{r}'(t)) = \left(-\partial_{x'_i} \partial_{x'_j} \psi_{\text{host}} \right) \Big|_{\mathbf{r}'=\mathbf{r}'(t)}, \quad (6)$$

and η is a free parameter ($\eta=1/400$ in this study, chosen from the values discussed in Grudić & Hopkins (2020) after validation tests). This allows KRIOS to resolve changes to the cluster mass and potential that occur faster than the two-body relaxation timescale. KRIOS evaluates Equation (6) directly from the various host potential components; see Appendix A.

KRIOS updates the SCF in two ways: “complete” refreshes, where α and b in Equation (4) are retuned and the SCF is reevaluated from scratch, and “intermediate” refreshes, where only particles that have become unbound from (or been recaptured by) the cluster are subtracted from (or added to) $a_{n\ell m}$ via the sum in Equation (3b). In this study, KRIOS executes a complete SCF refresh every 5 integration timesteps. We use an energy-based analog to the Lagrange radii, i.e., r_x is the smallest radius that encloses $x\%$ of the

energetically-bound particles³, to determine which particles are included in the Equation (3b) calculation. We only include particles where $r \leq r_{99.9}$ and refer to r_{100} , the smallest radius that encloses all energetically-bound particles, as the “bound radius” r_b .

Finally, the SCF is susceptible to finite- N noise (Hernquist & Ostriker 1992; Vasiliev 2015); this can be reduced by sampling multiple positions along the particles’ orbits during each integration. In Paper I, this was done with an equal number of samples per system timestep (based only on the relaxation timescale). As we are interested in changes that can occur on a dynamical timescale, here we collect orbital samples based on the cluster’s instantaneous dynamical time,

$$N_{\text{samples}} = \max \left(1, \left\lceil n_{\text{samples}, t_{\text{dyn}}} \times \frac{\Delta t_{\text{int}}}{t_{\text{dyn}}} \right\rceil \right), \quad (7)$$

where $n_{\text{samples}, t_{\text{dyn}}}$ is the desired number of samples per the instantaneous half-mass dynamical time (Binney & Tremaine 2008, hereafter B&T), i.e.

$$\left(\frac{t_{\text{dyn}}}{4.3451 \text{ Myr}} \right) = \left(\frac{M_{\text{cluster}}}{10^5 M_{\odot}} \right)^{-1/2} \left(\frac{r_{\text{hm}}}{10 \text{ pc}} \right)^{3/2}. \quad (8)$$

In this study, we set $n_{\text{samples}, t_{\text{dyn}}} = 1$.

2.3. Sampling Orbits Consistent with MW GCs

We must determine a set of orbit initial conditions consistent with the known population of MWGCs (e.g., Harris 2010; Piatti & Carballo-Bello 2020; Vasiliev & Baumgardt 2021; Chen et al. 2025b) and stellar streams (e.g., Malhan et al. 2022; Mateu 2023; Bonaca & Price-Whelan 2025) before highlighting the ways in which KRIOS models disagree with particle spray. The eccentricity and inclination are not necessarily conserved for orbits in non-Keplerian potentials, so we use conserved quantities that are readily accessible from observational data instead. Our set of orbits is shown in Figure 3. Recall that the energy E and z' -component of the angular momentum $L_{z'}$ are integrals of the motion for a test particle in a static and axisymmetric host potential. The energy can be expressed in terms of the angular momentum and meridional plane coordinates (Section 3.2.1 of B&T, Figure 3’s bottom panel):

$$E = \frac{1}{2}(v_{\varrho'}^2 + v_{z'}^2) + \psi_{\text{eff}}(\varrho', z'), \quad (9a)$$

$$\psi_{\text{eff}}(\varrho', z') \equiv \psi_{\text{host}}(\varrho', z') + \frac{L_{z'}^2}{2\varrho'^2}. \quad (9b)$$

³ We say the i^{th} particle is bound to the cluster if, via the standard N -body energy calculation in the cluster frame,

$$v_i^2 - \sum_{j \neq i} \frac{Gm_j}{|\mathbf{r}_i - \mathbf{r}_j|} < 0.$$

As this calculation is only performed every integration timestep, its contribution to the runtime is marginal.

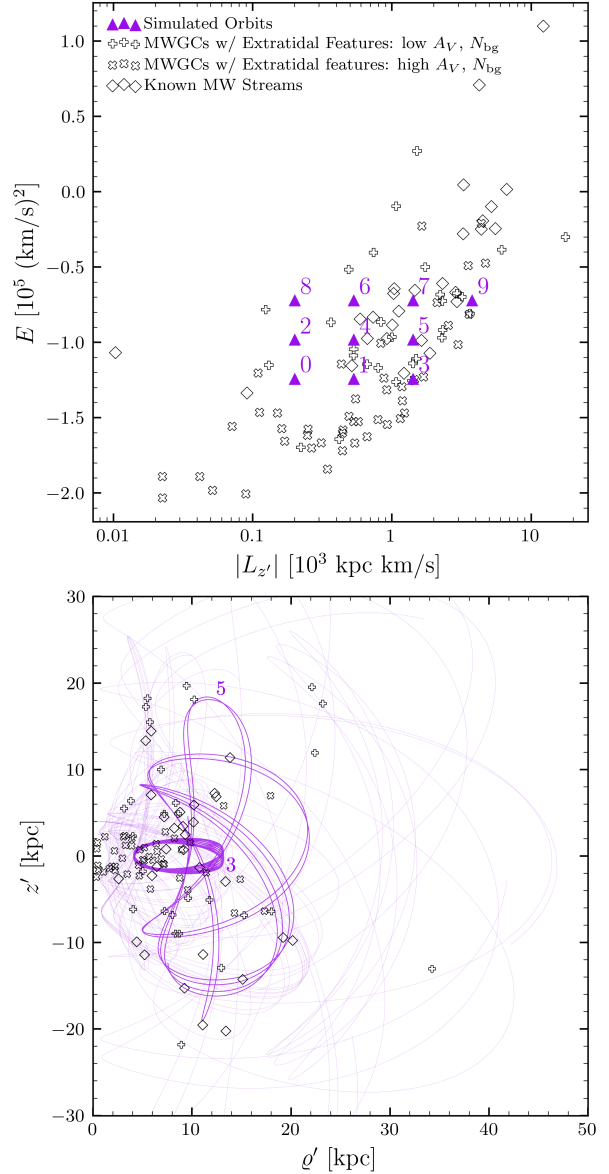


Figure 3. *Top panel:* The integrals of motion for the second set of Table 1 orbits compared to the known population of MW GCs (MWGCs; Harris 2010; Vasiliev & Baumgardt 2021; Chen et al. 2025b) and stellar streams (Table 1 of Malhan et al. 2022). Chen et al. (2025a) classifies MWGCs based on extinction A_V and background density N_{bg} . *Bottom panel:* The sampled orbits compared to the MWGCs and streams in the meridional plane, showing that our sample is biased toward orbits in the MW halo. Orbits 3 (closer to $z' = 0$) and 5 are boldened for illustrative purposes, as they are the stream models shown explicitly in Sections 3 and 4.

Therefore, if we start with a grid of $(|L_{z'}|, E)$ values (Figure 3’s top panel), we can identify nearby MWGCs in that space if we use MilkyWayPotential2022 (Price-Whelan et al. 2024) to estimate ψ_{host} . We sample the initial Galactocentric distance of each orbit, r'_{init} , based on the apogalacticon estimates— $r'_{\text{cluster}}(t_1)$ in Figure 2—for the

nearest MWGCs: $r'_{\text{init}} \sim \mathcal{N}(\mu_{r'_{\text{apo}}}, \sigma_{r'_{\text{apo}}}^2)$. This ensures that the cluster is not subject to substantive mass loss at the moment of initialization. The phase-space initial conditions, for a given set of $(L_{z'}, E, r'_{\text{init}})$ values, can then be sampled in the following way:

$$\alpha \sim \mathcal{U}(-\pi/2, \pi/2), \quad \beta \sim \mathcal{U}(0, 2\pi) \quad (10a)$$

$$\varrho'_{\text{init}} = r'_{\text{init}} \cos \alpha, \quad (10b)$$

$$\varphi'_{\text{init}} \sim \mathcal{U}(0, 2\pi), \quad (10c)$$

$$z'_{\text{init}} = r'_{\text{init}} \sin \alpha, \quad (10d)$$

$$v_{\varphi',\text{init}} = L_{z'} / \varrho'_{\text{init}}, \quad (10e)$$

$$v_{\varrho',\text{init}} = v \cos \beta, \quad (10f)$$

$$v_{z',\text{init}} = v \sin \beta, \quad (10g)$$

where $v \equiv \sqrt{2(E - \psi_{\text{eff}}(\varrho'_{\text{init}}, z'_{\text{init}}))}$. We only create retrograde orbits (i.e., $L_{z'} > 0$; Bonaca & Price-Whelan 2025) for simplification, which is permissible due to the axisymmetry of the host potential. An orbit with $t_{\text{end}} = 5$ Gyr and timestep $\Delta t = 0.1$ Myr is integrated using `gala` (Price-Whelan et al. 2024) to confirm that $1 \text{ kpc} \leq r'_{\text{peri}}$ and $10 \text{ kpc} \leq r'_{\text{apo}} \leq 60 \text{ kpc}$; see the bottom panel of Figure 3. If there are no (ϱ', z') pairs that satisfy $E \geq \psi_{\text{eff}}(\varrho'_{\text{init}}, z'_{\text{init}})$ and the $(r'_{\text{peri}}, r'_{\text{apo}})$ constraints, then the $(|L_{z'}|, E)$ pair is discarded.

While our method for sampling orbits starts directly from the integrals of motion, it is still useful to describe orbits in terms of their circularity (Abadi et al. 2003) and eccentricity, which can be defined in the following way:

$$\varepsilon \equiv \frac{L_{z'}}{L_{z',\text{circ}}(E)}, \quad (11a)$$

$$e \equiv \frac{r'_{\text{apo}} - r'_{\text{peri}}}{r'_{\text{apo}} + r'_{\text{peri}}}, \quad (11b)$$

where $L_{z',\text{circ}} = \varrho' \sqrt{2(E - \psi_{\text{host}}(\varrho', 0))}$ and ϱ' is the radius at which a circular orbit in the disk has energy E . The inclination of the cluster’s orbital plane with respect to the disk, $\cos i = L_{z'} / |\mathbf{L}|$, is not necessarily constant for a non-Keplerian potential. The properties of the orbits in Figure 3 can be found in Table 1.

3. RESULTS

We now run and compare ensembles of KRIOS, NBODY6++GPU, and particle-spray models of stellar streams on several different orbits in our Galaxy. In each ensemble, the stream’s progenitor cluster has an initial mass $M_{\text{cluster}} = 10^5 M_{\odot}$ and half-mass radius $r_{\text{hm}} = 10$ pc. The progenitor cluster in each KRIOS and NBODY6++GPU simulation is initialized with equal-mass point particles sampled—using the `COSMIC` population synthesis code (Breivik et al. 2020)—from a King (1966) distribution with

concentration parameter $W_0 = 5$ (e.g., Baumgardt & Makino 2003; Lamers et al. 2010). We generate several initial particle distributions for each cluster orbit and evolve each system forward for 5 Gyr. See Appendix B for the technical details of the NBODY6++GPU runs, as well as a description of the necessary corrections to the source files to use the `MWPotential2014` potential (Bovy 2015).

For our comparisons between NBODY6++GPU particle spray, and KRIOS (Section 3.3), we choose $N = 5 \times 10^4$ and $\psi_{\text{host}} = \text{MWPotential2014}$, and compare 1 KRIOS against an ensemble of 10 NBODY6++GPU runs and 10 particle-spray runs (to account for statistical fluctuations in our initial conditions and N -body integrations). For our detailed comparison between KRIOS and particle spray, we choose $N = 2 \times 10^5$ and $\psi_{\text{host}} = \text{MilkyWayPotential2022}$, and compare 2 KRIOS runs to 2 particle-spray runs. Note that we use `MWPotential2014` for our comparisons to NBODY6++GPU (as it was already implemented in that codebase), while our comparisons to particle spray use the more up-to-date `MilkyWayPotential2022`.

Using 128 CPU cores, the KRIOS runs took (6.6, 6.6, 21.1) hr versus (29, 38, 56) hr for NBODY6++GPU (see Appendix B for more details). The KRIOS runs with $N = 2 \times 10^5$ took between 5.9 and 22.1 hr on 192 CPU cores, with a median wall-clock time of 11 hr. Including a host potential in KRIOS runs introduces some computational overhead (Figure 14 of Paper I), but KRIOS is still a much faster alternative to direct N -body methods, and the speed advantage will only improve for larger N .

3.1. KRIOS Validation against NBODY6++GPU and Particle Spray

We consider three orbits in the `MWPotential2014` potential for validation: two circular orbits in the Galactic disk with radii $r'_0 = 5$ kpc and $r'_0 = 20$ kpc and one eccentric orbit that is misaligned with the disk. The initial tidal radii⁴ on these circular orbits are $r_t = 33.3$ pc and $r_t = 101.9$ pc, respectively. We refer to Table 1 for the validation orbits’ properties, Table A.2 for complete information on the phase-space initial conditions, and Appendix A for more details on the host potential.

We start by examining the cluster’s internal evolution: in Figure 4, we show the cluster’s Lagrange radii (top panel) and the number of unbound particles (a direct proxy for mass loss; bottom panel) for each of the validation orbits. There is good agreement in Lagrange radii between the KRIOS simulation and the NBODY6++GPU ensemble for the eccentric or-

⁴ For generic orbits, the tidal radius can be approximated as $r_t = (GM_c/\lambda_{1,e})^{1/3}$, where $\lambda_{1,e} = \lambda_1 - 0.5(\lambda_2 + \lambda_3)$, λ_1 is the largest eigenvalue of the tidal tensor (Equation (6)), and $0.5(\lambda_2 + \lambda_3)$ approximates the centrifugal term. See Appendix C of Pfeffer et al. (2018).

Table 1. The 13 orbits considered in this study. The first set is used for KRIOS validation against NBODY6++GPU (in the MWPotential2014 potential (which was already present in the N -body codebase) while the second set are for KRIOS comparisons to particle spray in the more up-to-date MilkyWayPotential2022 potential. We report each orbit’s integrals of motion, circularity ε , eccentricity e , mean/standard deviation of the inclination i , and for the MilkyWayPotential2022 orbits the times at which they reach perigalacticon and apogalacticon for the last time before the end of the simulation. We subtract off $\psi_{\text{MW2014}, \infty} \neq 0$ (Appendix A) when reporting the energies of the MWPotential2014 orbits such that bound orbits have negative energies. See Table A.2 for the initial phase-space coordinates accurate to eight decimal places.

Orbit ID	r'_{peri} [kpc]	r'_{apo} [kpc]	$t_{\text{last peri}}$ [Gyr]	$t_{\text{last apo}}$ [Gyr]	ε	e	i [deg]	$L_{z'}$ [10^3 kpc km/s]	E [10^5 (km/s) 2]
Circular 0 Test	5.00	5.00	–	–	1.00	0.00	0.0 ± 0.0	1.13	-1.30
Circular 1 Test	20.00	20.00	–	–	1.00	0.00	0.0 ± 0.0	3.95	-0.72
Eccentric Test	20.00	5.00	–	–	0.20	0.60	79.27 ± 0.68	0.33	-0.87
0	1.55	14.25	4.87	4.95	0.10	0.80	75.00 ± 3.45	0.20	-1.24
1	2.56	13.83	4.89	4.98	0.26	0.69	60.76 ± 3.68	0.53	-1.24
2	3.88	25.76	4.69	4.85	0.06	0.74	82.87 ± 0.45	0.20	-0.98
3	4.10	13.20	4.83	4.91	0.91	0.53	18.20 ± 3.29	1.41	-1.24
4	4.85	25.18	4.79	4.95	0.17	0.68	73.87 ± 0.70	0.53	-0.98
5	9.47	22.03	4.74	4.91	0.47	0.40	60.63 ± 0.48	1.41	-0.98
6	11.72	46.87	4.59	4.92	0.09	0.60	82.63 ± 0.05	0.53	-0.72
7	12.50	46.36	4.97	4.64	0.23	0.58	70.88 ± 0.11	1.41	-0.72
8	18.49	41.90	4.43	4.77	0.04	0.39	87.86 ± 0.01	0.20	-0.72
9	28.68	32.88	4.90	4.56	0.61	0.07	52.74 ± 0.10	3.76	-0.72

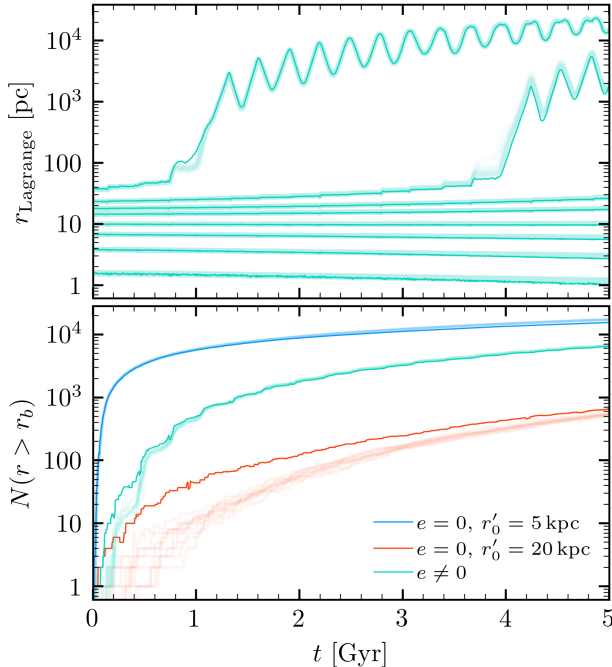


Figure 4. *Top panel:* The cluster’s Lagrange radii (i.e., the smallest radii that enclose $\{1\%, 10\%, 30\%, 50\%, 70\%, 80\%, 90\%, 99\%\}$ of the cluster mass) as a function of time for the eccentric validation orbit. The solid line is the KRIOS result and the shaded region represents the ensemble of NBODY6++GPU runs (10 for each orbit). *Bottom panel:* The number of particles outside the bound radius (defined in Section 2.2) as a function of time, color coded by orbit.

bit. The radii enclosing 90% and 99% of the cluster mass, for example, oscillate in accordance with the orbit. The connection between these panels is most clear at around $t=1$ Gyr,

where $N(r > r_b) \approx 500$ and the 99% Lagrange radius grows rapidly. The beginning of core collapse is evident, although this is a secondary effect for this cluster on this orbit. The timescale on which cluster orbits at the half-mass radius are modified by two-body relaxation is comparatively large for $N=5 \times 10^4$ and $r_{\text{hm}}=10$ pc (e.g., Spitzer 1987)

$$T_{\text{rlx}} = 0.138 \frac{N}{\ln \Lambda} \left(\frac{r_{\text{hm}}^3}{GM} \right)^{1/2}, \quad (12)$$

where $\ln \Lambda$ is the well-known Coulomb Logarithm (Equation 1.33b, B&T). The argument of the logarithm can be written in terms of a free parameter γ and the particle number N : $\Lambda=\gamma N$ (Chapter 14, Heggie & Hut 2003), with order-of-magnitude calculations using the virial theorem suggesting $\gamma=0.4$ (Spitzer 1987). In practice, many Monte Carlo (e.g., Rodriguez et al. 2022) and Fokker-Planck (e.g., Cohn 1980; Takahashi & Baumgardt 2012) codes treat γ as a free parameter set by tuning to direct N -body integrations. $\gamma=0.11$ has been shown to produce good agreement for isolated Plummer spheres without an external tidal field, while significantly smaller values produce good agreement when considering clusters with realistic stellar masses (e.g., $\gamma=0.01$ Rodriguez et al. 2018). For a King model of single-mass particles in a strong MW-like potential, we found KRIOS runs with $\gamma=0.6$ match the mass-loss rate of NBODY6++GPU for the eccentric orbit, and produces good agreement for the two circular orbits as well.

Having demonstrated good agreement between KRIOS and NBODY6++GPU for the internal evolution of the progenitor, we now compare the streams themselves. The first row of Figure 5 shows the distribution of two of the inte-

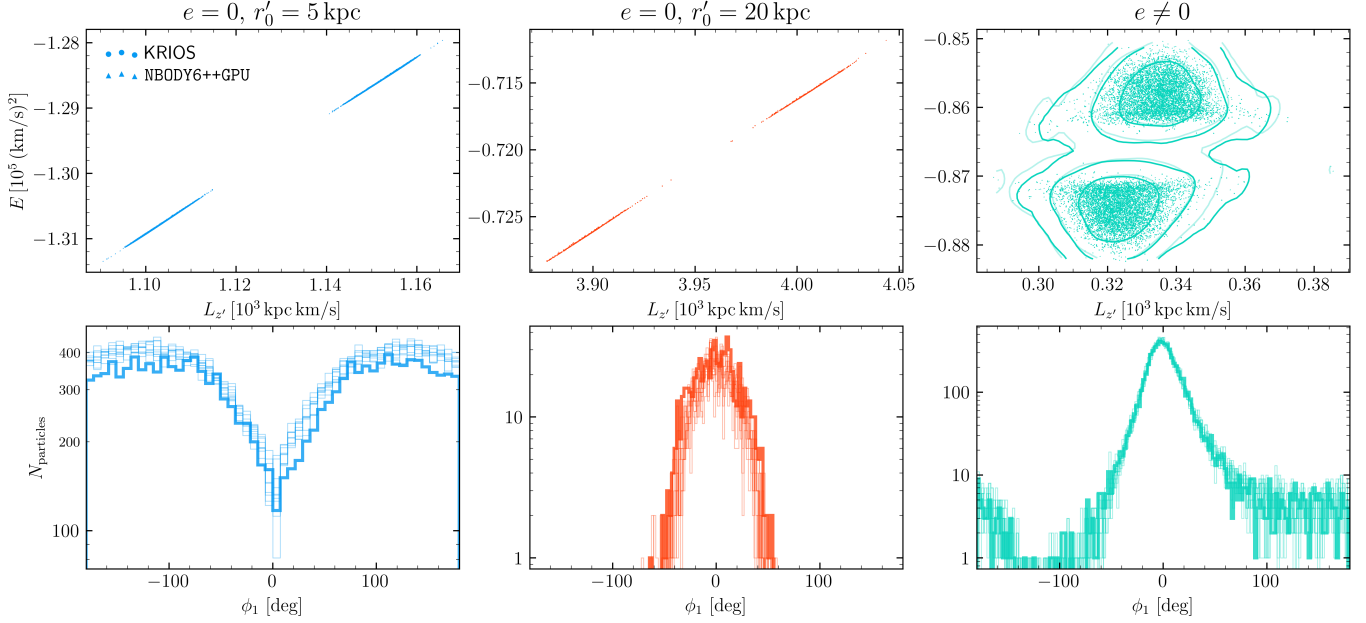


Figure 5. Integrals-of-motion and stream-track information for each of the validation models. *First row:* a scatter plot of the stream particles’ integrals of motion; contours encase 1σ , 2σ , and 3σ of the particles for the $e \neq 0$ test. *Second row:* Particle counts along the stream track. The solid lines represent the KRIOS result in each panel, while in the top-right panel the translucent contours represent the entire NBODY6++GPU ensemble. In the bottom row, each of the ensemble models are displayed separately. There are small discrepancies in the circular orbit tests consistent with the mass-loss rates shown in Figure 4, whereas there is good agreement for the eccentric orbit validation test.

grals of motion⁵ of the particles outside the bound radius of the cluster (defined in Section 2.2). The integrals of motion form a bimodal distribution, with the two peaks corresponding to the leading and trailing tails of the stream. The leading (trailing) tidal tail emanates from near the L_1 (L_2) Lagrange point (Fukushige & Heggie 2000), placing the escapers at lower (higher) $L_{z'}$ and E . The structure in the integral-of-motion distribution persists even when the stream traces a complete orbit and the tails are harder to distinguish (e.g. second row, first and third columns, Figure 5). The tidal tails from progenitors on circular orbits follow tracks with $E \propto L_{z'}$ (first and second panels, Figure 5), while the tidal tails from progenitors on eccentric and misaligned orbits present a more complicated picture (third panel, top row, Figure 5). However, the 1σ , 2σ , and 3σ contours of the KRIOS and NBODY6++GPU distributions are in good agreement here, despite being more diffuse in integrals-of-motion space than their circular-orbit counterparts.

The second row of Figure 5 shows the distribution of particles along the stream track (i.e. in ϕ_1) for KRIOS (darkest line) and each of the NBODY6++GPU runs (lighter lines). There is a small but consistent offset in the distribution for the circular orbit, which is due to a difference in the mass-

loss rate attributable to our $\gamma = 0.6$ setting. The eccentric orbit, which best resembles realistic GC orbits, shows broad agreement at all ϕ_1 .

To more quantitatively compare stream models, we compare the probability distribution functions predicted by KRIOS and NBODY6++GPU for $(L_{z'}, E)$ and (ϕ_1, ϕ_2) . We use two statistics, the Kullback-Leibler divergence (KLD; Kullback & Leibler 1951; Sanderson et al. 2015) and Earth Mover’s distance (EMD; Cohen & Guibasm 1999), to quantify the disagreement between a stream model (“A”) and its NBODY6++GPU counterpart (“NB”):

$$\text{KLD}_A = \sum_{x \in X} \rho_{\text{NB}}(x) \ln \frac{\rho_{\text{NB}}(x)}{\rho_A(x)} \quad (13a)$$

$$\text{EMD}_A = \min_{f \in \mathcal{F}(\rho_A, \rho_{\text{NB}})} \sum_{ij} f_{ij} d(x_i, x_j), \quad (13b)$$

where f_{ij} is the (i, j) element of the flow matrix f that maps ρ_A onto ρ_{NB} and $d(x_i, x_j)$ is the distance between those probability distribution elements. The KLD measures how different an approximate distribution ρ_A is from the ground-truth distribution ρ_{NB} . The EMD, on the other hand, measures the “cost” of manipulating ρ_A until it agrees with ρ_{NB} . The key difference between these metrics is that the KLD is ignorant to the approximation’s cost⁶ in a way that is mea-

⁵ Strictly speaking, a test particle in the host potential alone conserves E and $L_{z'}$, while the escapers are subject to small perturbations from the cluster potential.

⁶ This is especially true in cases where ρ_A goes to zero and ρ_{NB} does not, as this causes undefined behavior in the KLD calculation.

sured directly by the EMD. When estimating ρ , f , and d , we take a random subsample from the more-populated model such that both distributions are estimated from the same number of particles. This allows us to use Monte Carlo approximations to the KLD and EMD in equations 13a and 13b.

Figure 6 shows the 95% confidence intervals for the KLD and EMD, calculated for each of three comparisons:

- (i) Pairs of NBODY6++GPU runs from the ensemble compared to each other (first row). This number is a proxy for the minimum measurable KLD or EMD for the comparison, as they measure the intrinsic scatter between two different realizations of the same N -body initial conditions.
- (ii) KRIOS compared to each of the NBODY6++GPU runs (second row).
- (iii) Particle-spray runs (Plummer (1911) progenitor, Chen et al. (2025c) escaper distribution function) compared to NBODY6++GPU runs (third row).

The comparisons are calculated for each of the three test orbits (shown in different colors), and for the predicted distributions in $(L_{z'}, E)$ and (ϕ_1, ϕ_2) (sets divided by solid black horizontal lines).

In almost every case, KRIOS replicates the NBODY6++GPU prediction for the $(L_{z'}, E)$ distribution better than particle spray. This is more readily apparent in the EMD scores. In all but two cases—the KLD measured in (ϕ_1, ϕ_2) space for $r'_0 = 5$ kpc and the EMD measured in $(L_{z'}, E)$ space for $r'_0 = 20$ kpc—KRIOS has a better mean score than the corresponding ensemble of particle-spray runs. The improvement is especially large for the predicted distribution of the integrals of motion in the eccentric orbit case, and for the distribution along the stream track in the case of circular orbits. These results suggests that, overall, KRIOS can reproduce the relevant evolution and stream properties of full NBODY6++GPU runs in a fraction of the time, with a significantly higher fidelity than equivalent particle-spray runs.

3.2. Statistical and Systematic Variations between KRIOS and Particle-Spray Models

Having shown that KRIOS can produce streams with similar properties to those expected from NBODY6++GPU we can now explore a wider range of orbits and compare the predictions from KRIOS to those from various particle-spray methods. While it is possible for sets of particle-spray models to match the properties of NBODY6++GPU or KRIOS streams on average, it is not clear that they capture the statistical variation inherent in the N -body problem. All three stream-modeling methods exhibit inherent stochasticity due to the random sampling of the particles' initial positions

and velocities. But in the case of particle-spray codes, the stochastic “initial” conditions are introduced at the time of escape, as random draws from a distribution function of escaper properties. This ignores the well-known stochastic variation in the cluster evolution itself, which can produce changes in the cluster's mass and radii over time.

To that end, we compare predictions for the integral of motion distribution made by KRIOS and particle-spray ensembles over the wider range of orbits drawn to span the space of known GC orbits (Section 2.3; Figure 3). Figure 7 shows the statistical variation between independent KRIOS (triangles) and Chen25 particle-spray (circles) runs, as well as the systematic differences when these models are compared to each other (dashes). The models are compared at apogalacticon and in integrals-of-motion space using the EMD, which we found to be the more sensitive of the two metrics used in Section 3.3. Based on the results of those tests, we take the KRIOS prediction to be closer to the NBODY6++GPU run. Large differences between particle-spray and KRIOS thus highlight which orbits require a more accurate treatment of the escape physics than is achievable with particle-spray methods.

The EMD between two particle-spray models with different seeds (circle markers) is consistently lower than for KRIOS. This matches our expectation, as changing the random number generator's seed simply changes the starting point when drawing from a particle-spray model's constant distribution function, while in the KRIOS approach there is additional stochastic variation from the internal cluster dynamics. This suggests that ensembles of particle-spray models may underestimate stream-to-stream variability. On the other hand, an ensemble of KRIOS models is likely needed to confirm that an interesting feature of any particular stream is not an artifact of stochastic variation due to the cluster initial conditions or dynamical evolution. In future applications of KRIOS where a stream model is consistent with a dark matter subhalo flyby, for example, such considerations are critical.

As in Figure 6, the EMD between KRIOS and particle-spray models (lines with errorbars) shown in Figure 7 should be compared against the statistical variations between KRIOS runs to gauge the difference between the predictions. If the ratio between the two is high, then particle-spray models systematically deviate from KRIOS in a way that calls into question whether particle spray is accurate for these orbits.

3.3. Analysis of Systematic Differences between KRIOS and Particle Spray for Realistic Orbits

We now compare the streams generated by KRIOS to those generated by particle spray across the 10 Figure 3 orbits in the MWPotential2022 potential. In Figure 8, we show

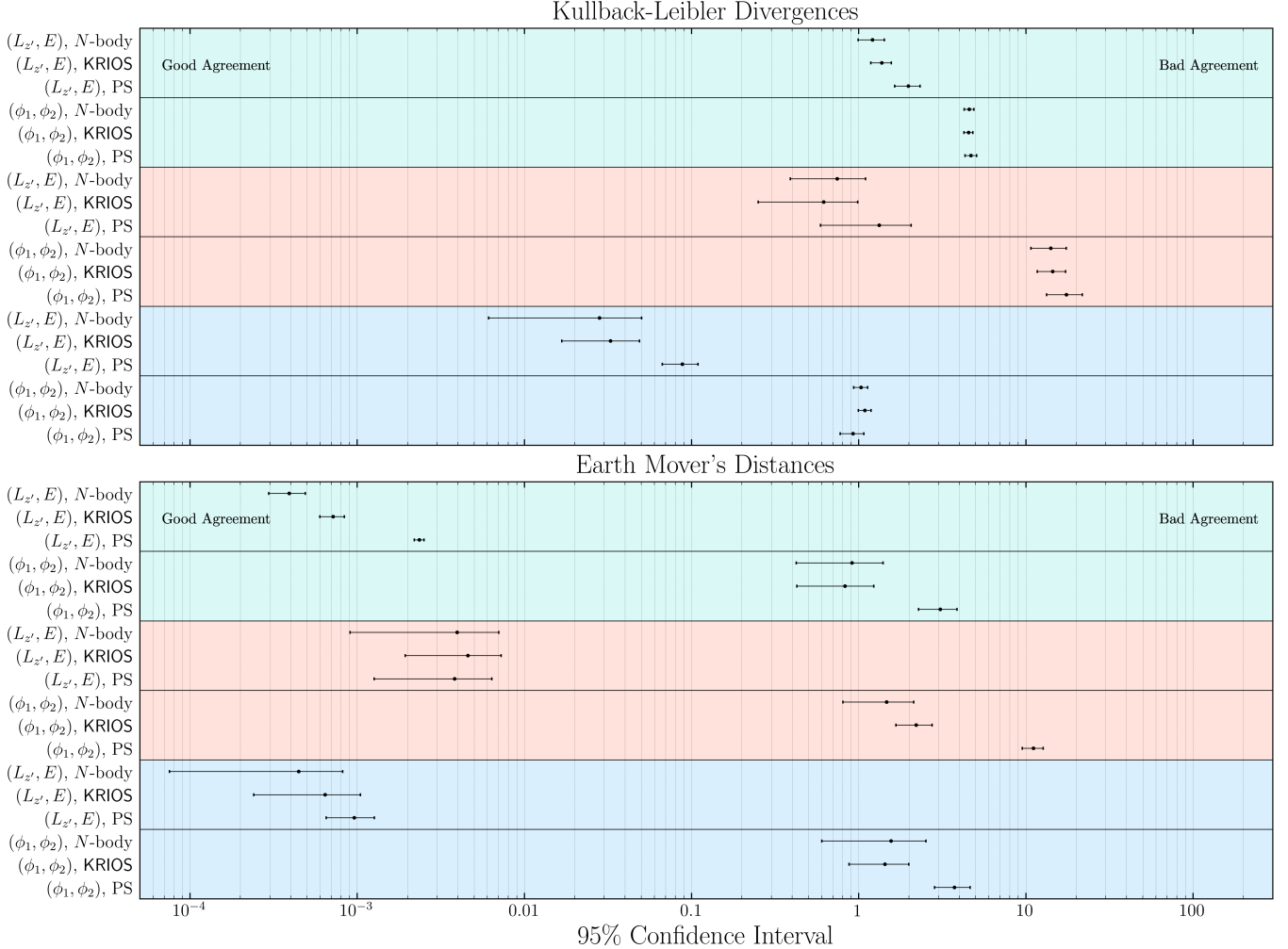


Figure 6. The Kullback-Leibler divergences and Earth Mover’s distances measured in $(L_{z'}, E)$ space and (ϕ_1, ϕ_2) space for each set of models (NBODY6++GPU, KRIOS, and particle spray). We show the 95% confidence intervals for (i) N -body scored against itself; (ii) KRIOS against N -body; (iii) particle spray (PS; Chen25 with a Plummer progenitor) against N -body. Each panel is color coded by orbit using the same scheme as Figures 4 and 5: green for $e \neq 0$, red for $r_0 = 20$ kpc, and blue for $r_0 = 5$ kpc. Values closer to the intrinsic distance between N -body runs (i; top row of each sub-panel) indicate better performance. KRIOS scores better than, or is statistically indistinguishable from, the ensemble of particle-spray models in all cases.

the ratio of the EMD KRIOS streams vs. particle-spray to the EMD between two different KRIOS runs in both (ϕ_1, ϕ_2) (top row) and $(L_{z'}, E)$ (bottom row) space. This ratio allows us to focus on the systematic agreement between the streams by normalizing to the statistical variation expected between cluster models with different realizations of the same initial conditions. We show these values calculated near their last perigalacticon passage (top row) and apogalacticon (bottom row). Overall, these results suggest that the added computational expense of creating stream models with a full N -body calculation is necessary when the stream is subject to strong tidal forces (i.e., small perigalacticon) or when it is tightly bound to the host galaxy (low E), especially if it is near the effective-potential barrier (high $|L_{z'}|$). Any inferences made about the properties of mock stellar streams made us-

ing particle-spray models (e.g., Holm-Hansen et al. 2025) should be applied with caution to streams that have these properties. The stellar stream associated with the M92 globular cluster (Thomas et al. 2020), for example, is susceptible both to modeling errors on the sky plane and in the integrals of motion. Streams like the Fjörm (Ibata et al. 2019b) system are less susceptible to integrals-of-motion errors, but, at apogalacticon, sky-plane variations will be pronounced. The Gunnthrá stream (Ibata et al. 2021), which may be debris from ω Cen (Cloud et al. 2024), appears to lie beyond the effective-potential barrier and is tightly bound to the Milky Way (as is its sister Fimbulthul stream, Ibata et al. 2019a); disagreement in stream integrals-of-motion is high in this region.

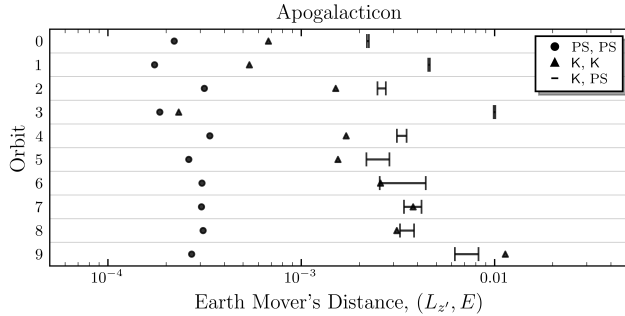


Figure 7. The integrals-of-motion EMD values for each orbit at the last apogalacticon passage. The circle markers represent particle spray’s statistical variation (same distribution function, different seeds) and the triangle markers represent KRIOS’s statistical variation (progenitor was initialized with a different random seed for each run). The errorbars show the minimum/maximum of the systematic variation between particle spray and KRIOS; there are $2 \times 2 = 4$ measurements.

On the other hand, several scientifically interesting streams can be robustly modeled with particle-spray according to these metrics. The GD-1 stream (Figure 1, Grillmair & Dionatos 2006), not shown in Figure 8, is currently near perigalacticon (Koposov et al. 2010) and has one of the largest $|L_{z'}|$ values of all known stellar streams (Bonaca et al. 2021). The Kshir stream, which has properties similar to GD-1 (Malhan et al. 2019), is shown in the bottom row of figures at high $|L_{z'}|$, similar to Orbit 9. Particle-spray models of streams on orbits of this kind will largely be consistent with KRIOS (and hence with NBODY6++GPU).

Interactions of streams with Galactic substructure, whether dark or baryonic, is thought to perturb the stream density $\rho(\phi_1)$ and velocity dispersion $\sigma(\phi_1)$ profiles along the stream track. It is critical that we understand which features of these profiles originate from the model assumptions, so that they are not mistaken for external perturbations. This is especially important given that several different escape prescriptions are commonly used in particle-spray models, yet there are very few tests of which prescriptions best reproduce $\rho(\phi_1)$ and $\sigma(\phi_1)$ for globular cluster streams. To examine differences in the predicted profile, we select particles that are unbound from the cluster and bin them in ϕ_1 from the inside out, starting at the progenitor, such that the number of particles in each bin $N_{\text{particles in bin}} \geq 100$ and the bin width $\Delta\phi_{1,\text{bin}} \geq 0.5$ deg. This binning strategy is chosen to accentuate differences in the $\rho(\phi_1)$ and $\sigma(\phi_1)$ profiles. Each distribution is computed from all particles in the stream (as opposed to Section 3.1, where the distributions were downsampled in order to calculate the KLD and EMD). We take many draws from each bin’s particles, detrend their velocities by subtracting a linear term $\bar{v}(\phi_1)$ within the bin, and then estimate the local 1D velocity dispersion $\sigma = \sqrt{\text{tr}(\Sigma)/3}$, where Σ is the covariance matrix of the detrended velocities. By

the central-limit theorem, this nonparametric bootstrapping method (Section 15.6.2 of Press et al. 2002) reduces the uncertainty in $\sigma(\phi_1)$ as we take more samples. We also calculate the average misalignment angle between the particles’ proper motions and unit vector tangent to the stream track, i.e. $\cos \theta_{\mu, \hat{t}}(\phi_1) \equiv \frac{1}{N} \sum_{i=1}^N (\hat{\mu}_i \cdot \hat{t}(\phi_{1,i}))$, which can also be used to probe the stream kinematics (e.g., Erkal et al. 2019). We parameterize $\phi_2(\phi_1)$ with a smoothed B-spline in order to calculate the tangent vector $\hat{t}(\phi)$ and hence the misalignment angle $\theta_{\mu, \hat{t}}(\phi_1)$.

As examples of stream structure that varies with the underlying modeling technique, we show the KRIOS and (Fardal15; Chen25) particle-spray models for Orbit 3 (Figure 9) and Orbit 5 (Figure 10). KRIOS and particle spray disagree on these orbits, more so for Orbit 3 than Orbit 5 (see Figures 7, 8). The latitude vs. longitude trends agree, which suggests that KRIOS and particle spray are equally capable of integrating particles forward in the same host potential. Variations in $\rho(\phi_1)$ are most notable near the progenitor, where different particle-spray distribution functions better replicate the density fluctuations predicted by KRIOS on different orbits. There is a notable demarcation between $\theta_{\mu, \hat{t}}(\phi_1)$ predictions near the progenitor for the Orbit 3 stream. The velocity dispersion profiles disagree as well, but this effect is seen most strongly in the tidal tails. The Fardal15 Orbit 3 stream, for example, systematically underestimates $\sigma(\phi_1)$. Both particle-spray models for the Orbit 5 stream are more spread out in ϕ_1 than the KRIOS model, which may be the source of the disagreement in $\sigma(\phi_1)$ and $\theta_{\mu, \hat{t}}(\phi_1)$. These results illustrate that subtle differences between models are imprinted on the predicted kinematics of the stream.

4. DISCUSSION

We showed in Section 3.3 that the predicted stream is sensitive to the implementation details of the underlying modeling technique. Particle-spray codes that sample escapers from some distribution function, for example, might ignore changes to the progenitor induced by the host potential or that mass loss is correlated with the strength of the tidal field. Additionally, stream-modeling techniques often assume the progenitor is spherically symmetric (e.g., CMC’s implementation of the Hénon method), which substantially affect the mass-loss rate—and hence also the predicted stream. This is particularly important in light of several recent works that examine streams from GCs simulated with CMC, ranging in complexity from GCs on circular orbits in a static and spherical MW (Weatherford et al. 2024; Weatherford & Bonaca 2025) to GCs on non-periodic orbits in an evolving and clumpy MW-like FIRE cosmological simulation (Panithanpaisal et al. 2025)—see also Grudić et al. (2023); Rodriguez et al. (2023). Here, we leverage KRIOS to explore potential discrepancies

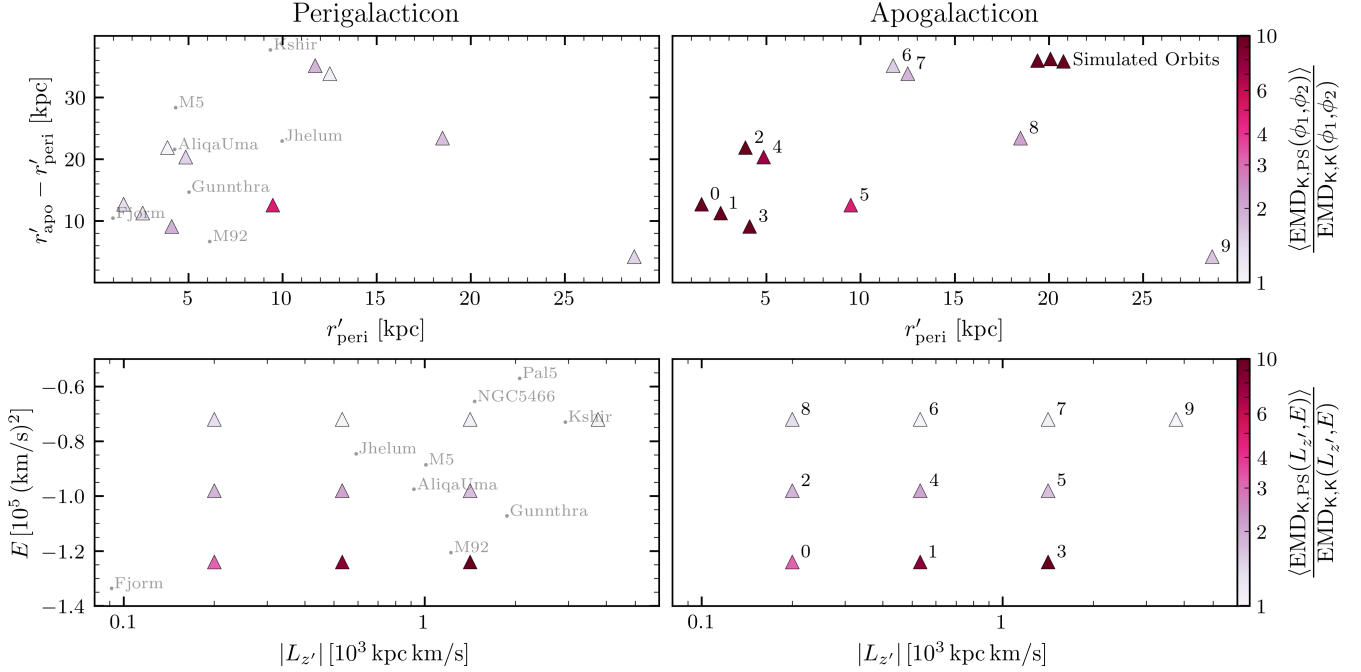


Figure 8. A comparison between the known MW stellar streams (labeled in the left column, Malhan et al. 2022) and simulated orbits (labeled in the right column) in apogalacticon/perigalacticon space (top row) and integrals-of-motion space (bottom row). Each orbit is color coded by the ratio $\langle \text{EMD}_{\text{K,PS}} \rangle / \text{EMD}_{\text{K,K}}$, which controls for statistical variations expected from KRIOS runs with the same initial conditions. Particle spray models show poorer agreement to KRIOS when the progenitor is subject to strong tidal fields or is tightly bound to the host.

between comparable stream-modeling techniques more concretely. We focus primarily on Orbit 3, as Figure 7 shows that this orbit shows the least stochastic scatter between similar KRIOS and particle-spray models, while showing significant disagreement between KRIOS and particle spray (as also seen in Figure 8).

4.1. A spherically symmetric progenitor is usually sufficient to model escaping stars

Though CMC simulations feature collisional dynamics and a particle-based GC potential, creation of model streams requires modeling the trajectories of escaping stars in post-processing since the full potential of the host galaxy is represented only by the tidal tensor. Bodies are removed from CMC upon achieving an orbital energy or apocenter sufficient for escape (often in the GC’s core), and then integrated in the mutual potential of the GC and its host galaxy. The GC potential is made analytic by fitting a Plummer sphere (Panithanpaisal et al. 2025)—or a three-component Plummer sphere to better reproduce the cores of evolved GCs (Weatherford et al. 2024; Weatherford & Bonaca 2025)—to the raw CMC potential and interpolating the fitting parameters coarsely in time (a few snapshots per half-mass relaxation time). The trajectories of stars forming a stream from a CMC cluster model thus only experience a fairly rough approximation of the true potential at the boundary between the GC and host galaxy. By comparison, particle-spray models often

assume a fixed Plummer progenitor, i.e. constant mass and half-mass radius. The self-consistent potential maintained by KRIOS, on the other hand (Equation (1a)), is tuned to the GC’s true configuration more accurately and at higher temporal resolution. Additionally, escapers are subject to the same SCF even after they leave the cluster. The model used in KRIOS is therefore more self-consistent and well-resolved on the relevant timescales within the cluster, and should be preferable to the CMC approach. We can use the structure of the SCF to test the effect of the assumption of a spherically symmetric cluster on the accelerations felt by escaping stars directly, since setting $\ell_{\text{max}} = 0$ is equivalent to forcing the cluster potential to be spherically symmetric as it is in CMC and many particle spray code.

We can probe the effectiveness of each progenitor model by comparing the accelerations from each model to those calculated by direct N -body summation. The top panel of Figure 11 shows the acceleration residuals ($\delta \mathbf{a} \equiv \mathbf{a}_{\text{model}} - \mathbf{a}_{N\text{-body}}$, Mukherjee et al. 2021; Arora et al. 2024) for different mean-field progenitor models, compared to the true values N -body accelerations. The Plummer progenitor that does not take cluster evolution into account (yellow curve), which is often used in particle-spray methods, poorly captures the particle accelerations. We see significant improvement if we use the instantaneous cluster mass and scale length for the Plummer potential (purple curve; e.g., Panithanpaisal et al. 2025). A multi-component Plummer

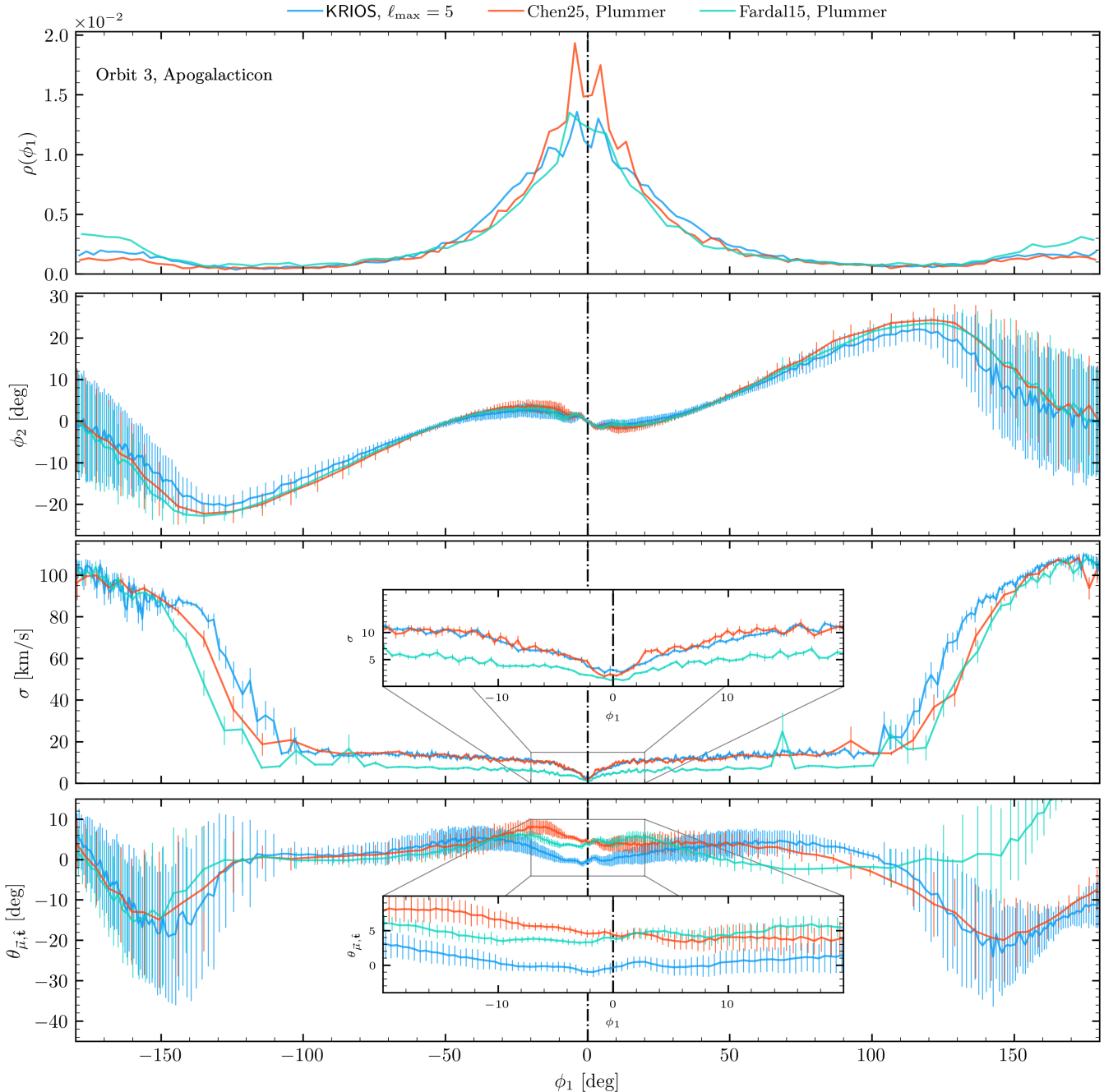


Figure 9. The Orbit 3 stream morphology (normalized density along the stream track $\rho(\phi_1)$, stream latitude ϕ_2) and kinematic (velocity dispersion σ , misalignment angle $\theta_{\mu, t}$) information for each model near the last apogalacticon passage. The fiducial ($n_{\max} = 10$, $\ell_{\max} = 5$) KRIOS model is compared against particle-spray models with a Plummer progenitor and different escaper distribution functions ([Fardal15](#); [Chen25](#)). The dashed line at $\phi_1 = 0$ indicates the progenitor location and inset panels zoom in to regions with notable differences between models. The largest disagreements are the density and misalignment angle near the progenitor, as well as the velocity dispersion and misalignment angle in the tails. This stream's velocity dispersion is systematically underestimated when using the [Fardal15](#) distribution function and the [Chen25](#) distribution function overestimates the central overdensity.

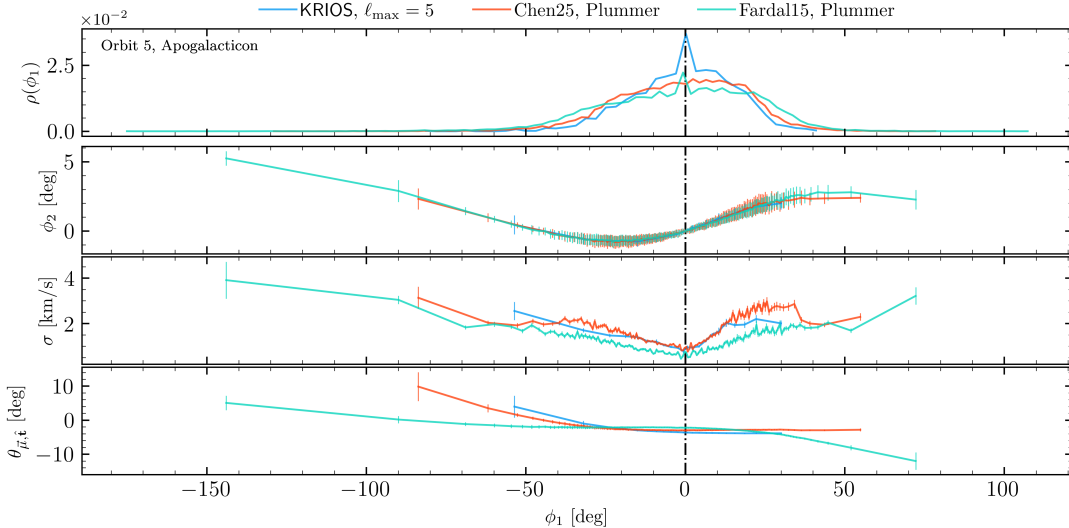


Figure 10. The same information as Figure 9, but for the Orbit 5 stream at last apogalacticon. This is an orbit where particle spray and KRIOS are in moderate disagreement (see Figure 8). This stream is dynamically colder than the one displayed in Figure 9; the velocity dispersion is $\sigma \lesssim 6$ km/s and the misalignment angle $\theta_{\mu,i} \lesssim 10$ deg everywhere along the stream. The particle-spray are more diffuse longitudinally, leading to an underestimation of $\rho(\phi_1)$ near the progenitor and variations in the $\theta(\phi_1)$.

potential fit would result in further improvement (Weatherford et al. 2024), and using CMC’s exact spherical-shell potential $\psi_{\text{cluster}} = -\frac{GM_{\text{enc}}(r)}{r}$ (dotted green curve) is better still, agreeing well with the spherically symmetric KRIOS SCF (red curve). The fiducial KRIOS profile ($\ell_{\text{max}} = 5$; blue curve) best reproduces the target accelerations. By construction, it is able to resolve tangential acceleration components in a way that spherically symmetric fields cannot. The bottom panel of Figure 11 shows how the accelerations, expressed as the gradient of the potential in Hénon units, compare to the fiducial model. Here, we see the Plummer-sphere approximations (both fixed and evolving) separate from the non-Plummer-sphere approximations in the GC’s core, as well as how the zeroth-order mode of the SCF disagrees with the spherical-shell potential for $r \lesssim 0.5 r_{\text{core}}$.

Figure 12 shows the impact of different progenitor prescriptions on the stream, which again are slight disagreements in $\rho(\phi_1)$ and $\sigma(\phi_1)$. There is no clear connection between improving the treatment of the progenitor potential—from no progenitor at all, to a Plummer model, to an SCF model—and the accuracy of stream density, morphology, or kinematics. Interestingly, it is the intermediate model (Plummer) that has the worst velocity dispersion agreement with KRIOS in the tails, but best replicates the density variations near the progenitor. The implication here is that there is an upper limit on the degree to which particle spray can be improved with more accurate initializations of a fixed progenitor. However, related improvements to modeling the progenitor’s internal *dynamics*, such as explicit treatment of strong encounters (in the process of being added to KRIOS), still

can substantially affect stream properties (e.g., Gieles et al. 2021; Weatherford & Bonaca 2025).

4.2. Spherically (a)symmetric KRIOS progenitors produce statistically similar streams

The $\psi_{\text{eff}}(\mathbf{r}) = E_J$ surface through which a bound particle with Jacobi integral $E_J = \frac{v^2}{2} + \psi_{\text{eff}}$ cannot pass (i.e., the zero-velocity surface, B&T) is not spherically symmetric. Particles escape primarily in the vicinity of the L_1/L_2 Lagrange points, especially those whose Jacobi integral is only marginally above the escape threshold (e.g., Fukushige & Heggie 2000; Weatherford et al. 2024). Figure 2 of Chen25, which shows the normal distribution of escapers' spherical phase-space coordinates from N -body runs, provides further evidence of escape anisotropy.

The asphericity of the GC's mass distribution can be measured by the power in each of the ℓ modes, computed as $E_\ell = \sum_{nm} |a_{n\ell m}|^2$ (Equation D36 of [Paper I](#)), where $\{a_{n\ell m}\}$ are the SCF's basis coefficients. The GC is spherically symmetric if $E_\ell = 0$ for all $\ell > 0$. Figure 13 compares the eccentric validation model's SCF ℓ -mode power spectrum and the tidal tensor's Frobenius norm $\|T\|$, all normalized by their initial values, as a function of time. This time-series data demonstrates how KRIOS clusters evolve when coupled to external tidal fields. The $\ell=0$ monopole term loses power as the cluster loses mass. The $\ell=1$ dipole term measures how well the SCF is centered on the cluster.⁷ The asphericity

⁷ If the center of mass were used instead of the location that maximizes $a_{nlm} = a_{000}$, for example, there would be more power in the dipole term (in contrast with what is stated in Section 2.4 of B&T).

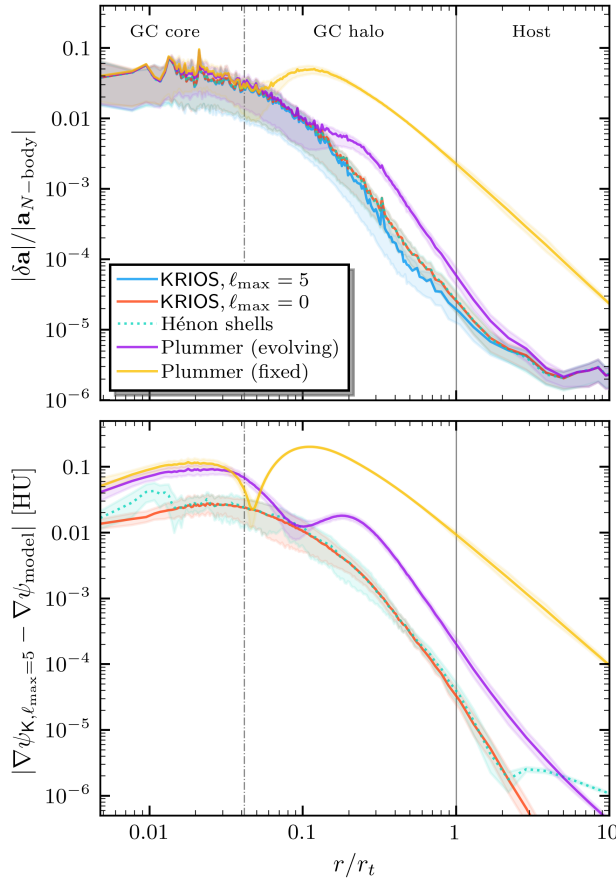


Figure 11. The residuals for the particle data from the last perigalacticon passage of the Orbit 3 system using different ψ_{cluster} models. The shaded regions show the 1σ spread for that bin. *Top panel:* The acceleration residuals when compared against direct N -body summation. The spherically asymmetric KRIOS potential is the only one capable of resolving tangential accelerations, and is generally the most successful at replicating the N -body acceleration profile outside of the core (black dashed line). This is especially important near the tidal boundary (black solid line⁴), where the effective-potential contributions from the host potential and centrifugal term are equally important. *Bottom panel:* The gradient of the fiducial cluster potential (KRIOS, $\ell_{\text{max}}=5$) compared to other cluster potential models, where the variations between the various mean-field approximations are more clear. The fixed Plummer potential (yellow curve), which is often used in particle-spray models, is a comparatively inaccurate approximation.

of the system is represented by the $\ell \geq 2$ modes (Hernquist & Ostriker 1992; Weinberg 1996; Vasiliev 2019). A significant amount of power is deposited in the $\ell=2$ quadrupole term, which is an instantaneous measure of the cluster’s oblateness (Hill & Wheeler 1953), during each tidal shock (either at perigalacticon or during a disk passage). Aspherical distortions of this kind are qualitatively consistent with MWGC observations (Chen & Chen 2010).

Despite this measurable change in the cluster’s oblateness, the integrals-of-motion and sky-plane EMD scores between the fiducial $\ell_{\text{max}}=5$ models and the models where spherical symmetry is enforced ($\ell_{\text{max}}=0$) have the following ranges when evaluated at apogalacticon:

$$\langle \text{EMD}_{K5,K0} \rangle \in \begin{cases} (0.5, 1.4) & (L_z', E), \\ \text{EMD}_{K5,K5} & (0.7, 1.9) \quad (\phi_1, \phi_2). \end{cases}$$

This suggests that stream models produced by Hénon-based N -body codes like CMC will only suffer from mild disagreement due to the assumed spherical symmetry of the progenitor, as long as the progenitor is properly incorporated when calculating escaper dynamics (Section 4.1). We have not made direct comparisons between CMC and KRIOS models, so the degree to which their predictions for stream substructure (e.g., gaps, spurs) agree warrants investigation in future studies.

4.3. Mass-loss Rate Variability in Stream Modeling

Our particle-spray models, to this point, have assumed a constant mass-loss rate (i.e., escapers drawn from the (Fardal15; Chen25) distribution functions at each timestep). Here, we consider the impact of a variable mass-loss rate. The third panel of Figure 2 in Panithanpaisal et al. (2025) shows that the number of ejected particles peaks sharply during perigalacticon passages, which is corroborated by KRIOS (see the green curve in the second panel of Figure 4). Variable mass-loss rates can be added to particle-spray models by passing an array of particle counts to be released during each timestep to the relevant `gala` stream-generation method⁸ or through post-processing of the stream data itself (e.g., Pearson et al. 2024). Candidate variable mass-loss rates include $\dot{M}(t) \propto M(t)^a \Omega(t)^b r_{\text{hm}}(t)^c$ (fit to observational data in Chen et al. 2025b), where $\Omega(t)$ increases during perigalacticon passages, and Fardal15, which uses an analytic prescription for the mass-loss rate as a function of the orbit’s radial phase to build its distribution function. The latter is more applicable to particle-spray methods that do not track the progenitor mass or half-mass radius. Neither prescription accounts for disk shocks that heat up the progenitor, and by default `gala` assumes a constant mass-loss rate.

Figure 14 shows the mass-loss rate in the Orbit 3 and Orbit 5 KRIOS simulations (blue) for three complete orbits and compares them to the following mass-loss prescriptions: constant (black dashed line), Equation 16 of Fardal15 (green), mass loss directly proportional to the tidal tensor’s Frobenius norm (red), and mass loss proportional to the mass-loss history from the KRIOS data (purple). A constant mass-loss

⁸ <https://gala.adrian.pw/en/latest/dynamics/mockstreams.html>

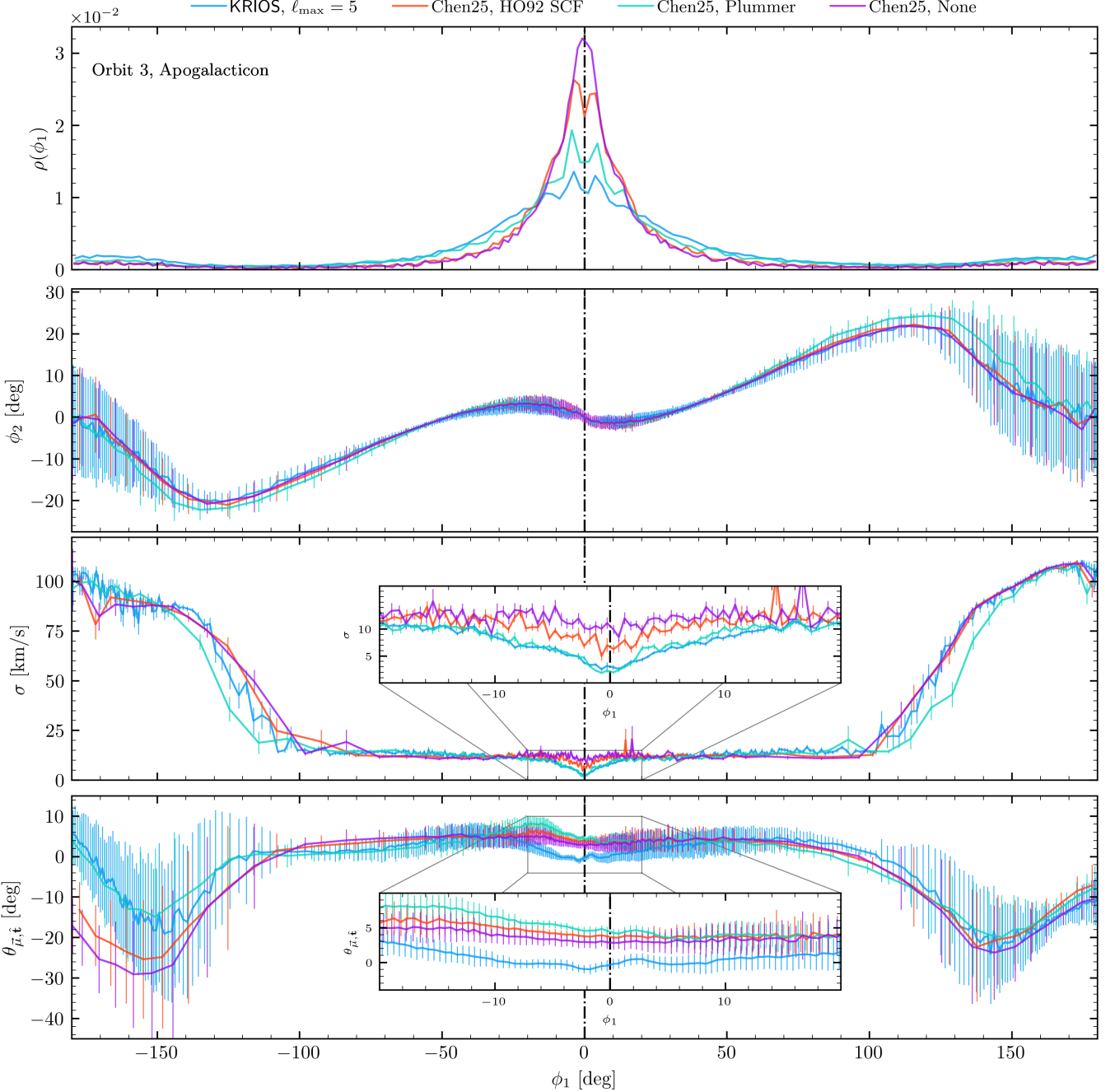


Figure 12. The fiducial KRIOS model for the Orbit 3 stream compared to three Chen25 models near the last apogalacticon passage: one with an SCF progenitor (Hernquist & Ostriker 1992, $n_{\max} = \ell_{\max} = 2$), one with a Plummer progenitor, and one with no progenitor. There does not appear to be immediate improvement in the modeling with improved treatment of the progenitor, assuming that the progenitor is fixed.

rate is clearly a poor fit to the Orbit 3 data, as the peak mass-loss rate at perigalacticon (which coincides with a disk passage, see Figure 3) is $\sim 10\times$ the average. Additionally, the mass-loss rate is suppressed after these peaks; this is likely attributable to the unavailability of easily stripped particles that are replenished through continued relaxation when the cluster is subject to comparatively weak tidal forces. For the Orbit 5 model, there are only $\lesssim 5$ particles ejected per in-

tegration timestep, so a constant mass-loss rate heuristic is likely acceptable in this context. The tidal tensor captures disk shocks (see the peaks in the red curve), which might make it suitable as a generalized mass-loss rate prescription.

Figure 15 shows how these mass-loss rates manifest in models of the Orbit 3 stream. The blue curve shows the fiducial KRIOS $\ell_{\max} = 5$ model that is also shown in Figures 9 and 12. The green curve shows the particle-spray model

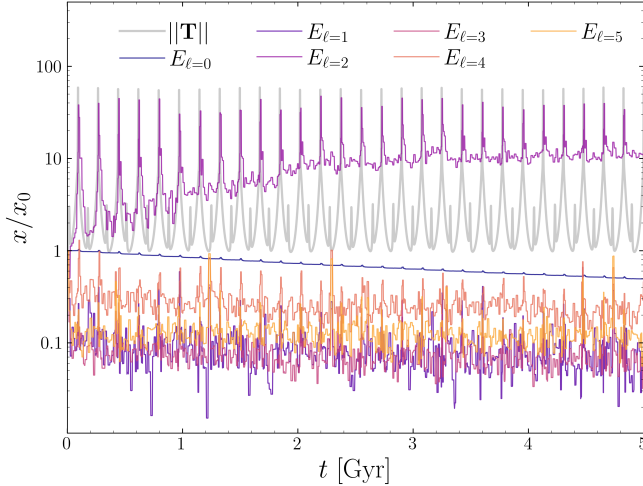


Figure 13. The power in each SCF ℓ mode (i.e., $E_\ell = \sum_{nm} |a_{n\ell m}|^2$) compared to the tidal tensor’s Frobenius norm for the Orbit 3 KRIOS run. The $\ell=2$ quadrupole term, which measures the cluster’s oblateness, is correlated with the strength of the tidal field. Discontinuities in the tidal field strength are attributable to perigalacticon and disk passages.

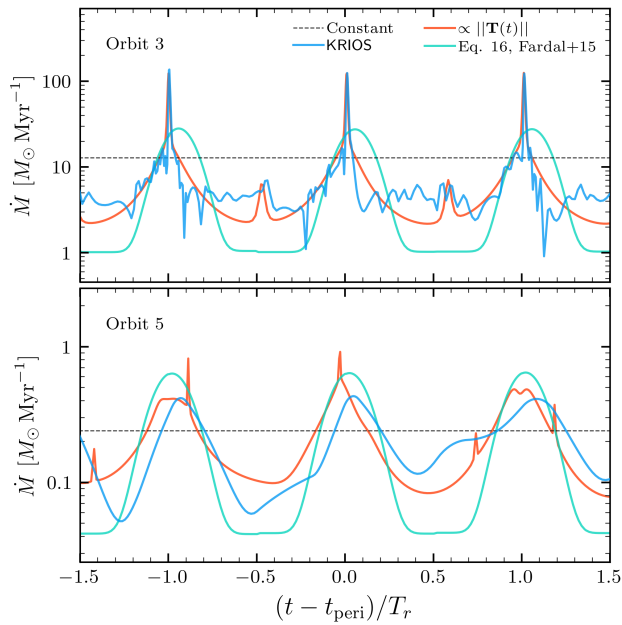


Figure 14. The mass-loss rate for three radial periods of the Orbit 3 and Orbit 5 KRIOS models ($t_{\text{peri}} \sim 2.5$ Gyr). The KRIOS mass-loss rate estimate is a spline fit to the $\Delta M / \Delta t$ data from each integration timestep. The black dashed line represents the constant mass-loss rate typically used in particle-spray studies. The green curve shows Equation 16 of Fardal15, where the peak mass-loss rate is slightly offset from perigalacticon. The red curve shows a hypothetical mass-loss rate proportional to the tidal tensor’s Frobenius norm, which accommodates disk shocks.

with [Chen25](#) distribution function and Plummer progenitor (see Figure 12) where the mass-loss rate is constant, and the red curve shows the same particle-spray model where the mass-loss rate is set by passing the $||T(t)||$ time-series data to the stream-generation method. The purple curve’s disagreement with the KRIOS model is likely due to all of the other modeling differences (e.g., static Plummer sphere progenitor and escaper distribution function). Further investigation is needed into variable mass-loss rate prescriptions that better replicate the numerical experiments we have carried out with KRIOS in this study, e.g. ones that take the recent history of the tidal tensor along the orbit into account.

5. CONCLUSIONS

In this paper, we expand the scope of the KRIOS hybrid N -body code that was recently introduced in [Paper I](#) by modeling tidal debris from globular clusters orbiting a host galaxy. Realistic MW potential models are used to validate KRIOS against known, successful stream-modeling techniques. There is good agreement between KRIOS and NBODY6++GPU when the respective codes model the internal evolution of GCs in an external tidal field, as well as their resultant debris. It is found that, on an orbit consistent with realistic MWGC orbits, KRIOS replicates the sky-plane and integrals-of-motions distributions from comparable NBODY6++GPU runs.

5.1. Conclusions for Stream Modelers

We use a collection of [MilkyWayPotential2022](#) sample orbits, spanning the region of orbit space occupied by known MW streams, to test how KRIOS and particle-spray models might disagree in scenarios similar to those found in the observational data. Particle-spray results deviate from KRIOS in the following scenarios:

- The GC is subject to strong tidal forces during its orbit, characterized by small perigalacticon and apogalacticon distances. The Fjörm and M92 streams are examples of such systems. Differences in the stream’s distribution on the sky plane are most apparent when they are near apogalacticon.
- The GC is tightly bound to the host galaxy. This applies to circular (M92, Gunnhrá) and radial (Fjörm) orbits alike. Systems of this kind lead to disagreements in how well the integrals of motion of the stream stars are conserved.

The most common form of disagreement between KRIOS and particle-spray stream models are in the resolution of density fluctuations near the progenitor and the velocity dispersion of the tails far from the progenitor. Inferences made about the morphology of the GC’s extratidal features or the

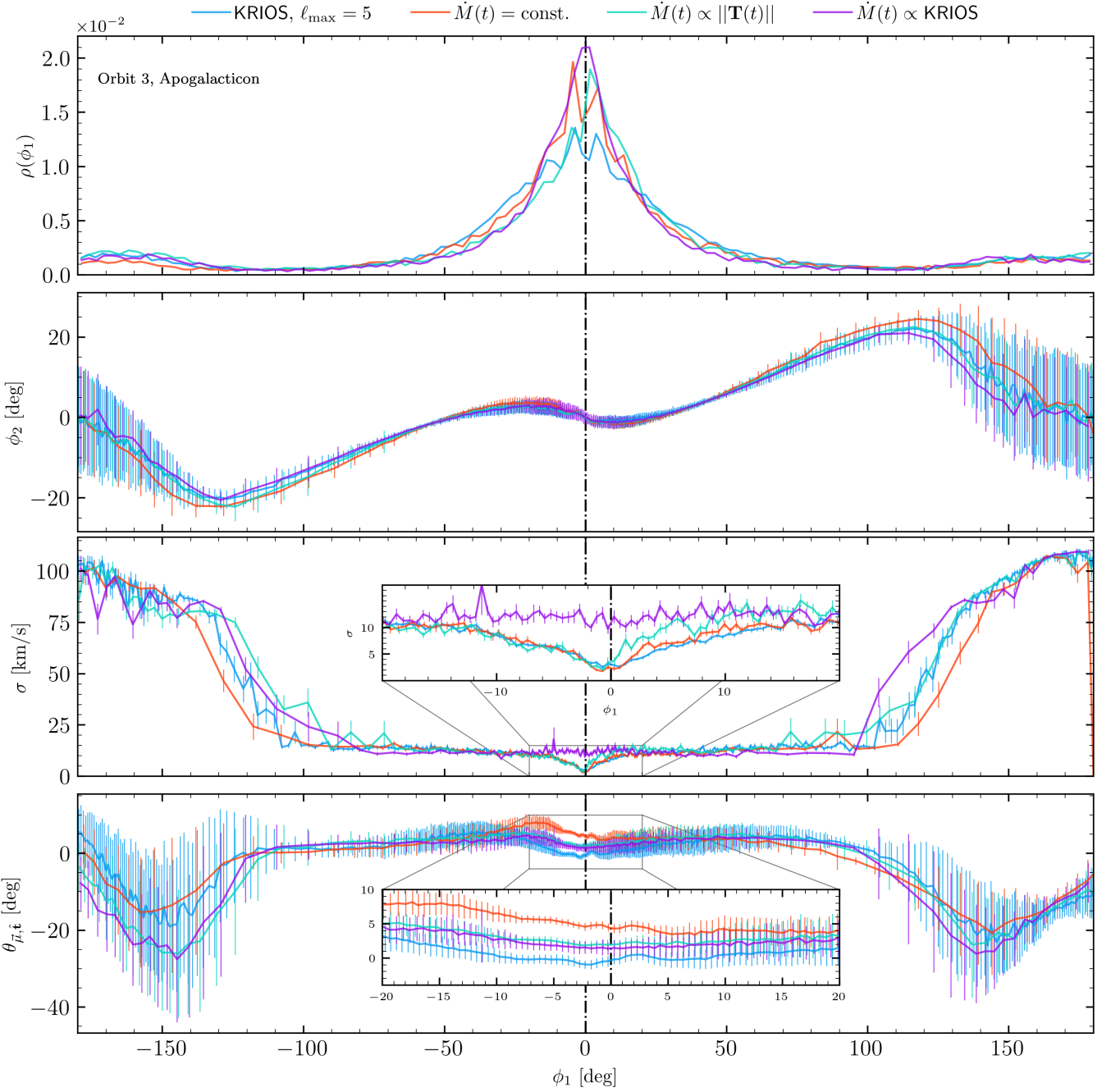


Figure 15. The fiducial KRIOS model for the Orbit 3 stream compared to three [Chen25](#) models with a Plummer progenitor: one with a fixed mass-loss rate (red, see Figure 9), one with a variable mass-loss rate proportional to the tidal tensor's Frobenius norm (green), and one with a variable mass-loss rate collected directly from the KRIOS data (purple). There is a larger spread in the tail velocity dispersions than when the progenitor is modified (Figure 12) and the density fluctuations near the progenitor are not modeled correctly by particle spray even with more realistic mass-loss rates.

kinematics of sparsely populated regions in the GC streams should consider whether the progenitor physics are appropriately taken into account. Even when particle spray reproduces the stream (as measured statistically by the KLD or EMD), its internal structure depends on the particle-spray implementation (Section 3.3; Figures 9 and 10). Several different escaper distribution functions and mass-loss prescriptions should be considered in order to eliminate these as explanations for substructure. The mass-loss rate is computed self-consistently with KRIOS, so no prescription is needed. We find that there are limitations to more sophisticated models of a fixed progenitor in particle-spray methods; rather, it is likely more important to incorporate time-dependent progenitors that accommodate variable mass-loss rates, and to consider the impacts of a realistic stellar mass function and ejection via strong encounters (see, e.g., Gieles et al. 2021; Grondin et al. 2024; Weatherford & Bonaca 2025).

Assuming a spherical model of the progenitor cluster, as is done in CMC, is sufficient, in most cases, to model the escape of stars from the cluster (Section 4.1) and resolve the internal cluster dynamics (Section 4.2) when predicting the density, velocity dispersion, and misalignment along the stream. This may not be the case for all clusters, e.g. if there is internal rotation (Chen & Chen 2010; White et al. 2025). In the future, we plan to implement time-dependent host potentials from cosmological simulations, as there are known defects with stream models in a smooth (e.g., Bonaca et al. 2014) or static (e.g., Arora et al. 2022) host potential. This will be the foundation for future cosmological stellar stream catalogs (e.g., Panithanpaisal et al. 2025; Holm-Hansen et al. 2025), where the progenitor’s N -body code is designed specifically for this use case.

KRIOS runs are terminated once there are only 100 particles in the core (i.e., core collapse, see Section 2). $N \leq 4$ microphysics (Heggie & Hut 2003) are not yet accounted for, e.g. the production of binary star systems (e.g., Atallah et al. 2024), which are critical to modeling the post-collapse evolution of globular clusters. Figure 2 of Weatherford et al. (2023) demonstrates that these phenomena have a tangible impact on stream production as well, which necessitates their inclusion in future implementations of KRIOS. In future work, we plan to include both three-body binary formation and strong encounters between single and binary stars. We will also model stellar/binary evolution with a realistic initial mass function (Kroupa 2001; Baumgardt et al. 2023) using the COSMIC population-synthesis code (Breivik et al. 2020).

ACKNOWLEDGMENTS

We thank Dany Atallah for helpful discussions that improved the quality of the manuscript. This work was supported by the National Science Foundation under Grants

Numbers AST-2510181 to the University of North Carolina, AST-2510183 to Northwestern University, and by NASA ATP Grant 80NSSC24K0687. CR also acknowledges support from an Alfred P. Sloan Research Fellowship and a David and Lucile Packard Foundation Fellowship. BTC was partially funded by the North Carolina Space Grant’s Graduate Research Fellowship. TS gratefully acknowledge the support of the NSF-Simons AI-Institute for the Sky (SkAI) via grants NSF AST-2421845 and Simons Foundation MPS-AI-00010513. TS was also supported by NASA through grant 22-ROMAN22-0013. This work was supported by a research grant (VIL53081) from VILLUM FONDEN. CR, KT, and RS also thank the organizers of the workshop “Interconnections between the Physics of Plasmas and Self-gravitating Systems”, supported by NSF Grant PHY-2309135 to the Kavli Institute for Theoretical Physics (KITP). This work was also co-funded by the European Union (ERC, Beyond-STREAMS, 101115754) grant. Views and opinions expressed are however those of the author(s) only and do not necessarily reflect those of the European Union or the European Research Council. Neither the European Union nor the granting authority can be held responsible for them.

We would like to thank the University of North Carolina at Chapel Hill and the Research Computing group for providing computational resources and support that have contributed to these research results. We thank Stéphane Roubertol for the smooth running of the Infinity cluster of the Institute of Astrophysics of Paris, where the NBODY6++GPU runs were performed.

KRIOS simulations, and their subsequent analyses, depend on the following software packages: GNU Compiler Collection⁹, GNU Scientific Library (GSL, Gough 2009), OpenMP (Dagum & Menon 1998), numba (Lam et al. 2015), NumPy (Harris et al. 2020), SciPy (Virtanen et al. 2020), pandas (McKinney 2010), Matplotlib (Hunter 2007), Astropy (Astropy Collaboration et al. 2018), gala (Price-Whelan et al. 2024), galpy (Bovy 2015), Python Optimal Transport (POT, Flamary et al. 2021).

DATA DISTRIBUTION

There is a public GitHub repository (https://github.com/BrianTCook/krios_ii_paper_supplement) containing a subset of the data presented in this paper, as well as a Jupyter notebook that produces relevant observables from that data. Additional data will be made available upon request to the authors.

To facilitate the reproducibility of our NBODY6++GPU results and allow its use of the MWPotential2014 external field, we created a fork of the original NBODY6++GPU repository containing these corrections

⁹ <https://gcc.gnu.org/>

(<https://github.com/KerwannTEP/Nbody6ppGPU>). Addi-

tionally, we provide pre- and post-processing scripts at <https://github.com/KerwannTEP/NB6-MW2014-Tools>.

REFERENCES

Aarseth, S. J. 1999, PASP, 111, 1333, doi: [10.1086/316455](https://doi.org/10.1086/316455)

Abadi, M. G., Navarro, J. F., Steinmetz, M., & Eke, V. R. 2003, ApJ, 597, 21, doi: [10.1086/378316](https://doi.org/10.1086/378316)

Amorisco, N. C. 2015, MNRAS, 450, 575, doi: [10.1093/mnras/stv648](https://doi.org/10.1093/mnras/stv648)

—. 2017, MNRAS, 464, 2882, doi: [10.1093/mnras/stw2229](https://doi.org/10.1093/mnras/stw2229)

Arora, A., Sanderson, R. E., Panithanpaisal, N., et al. 2022, ApJ, 939, 2, doi: [10.3847/1538-4357/ac93fb](https://doi.org/10.3847/1538-4357/ac93fb)

Arora, A., Sanderson, R., Regan, C., et al. 2024, arXiv e-prints, arXiv:2407.12932, doi: [10.48550/arXiv.2407.12932](https://doi.org/10.48550/arXiv.2407.12932)

Astropy Collaboration, Price-Whelan, A. M., Sipőcz, B. M., et al. 2018, AJ, 156, 123, doi: [10.3847/1538-3881/aabc4f](https://doi.org/10.3847/1538-3881/aabc4f)

Atallah, D., Weatherford, N. C., Trani, A. A., & Rasio, F. A. 2024, ApJ, 970, 112, doi: [10.3847/1538-4357/ad5185](https://doi.org/10.3847/1538-4357/ad5185)

Baumgardt, H., Hénault-Brunet, V., Dickson, N., & Sollima, A. 2023, MNRAS, 521, 3991, doi: [10.1093/mnras/stad631](https://doi.org/10.1093/mnras/stad631)

Baumgardt, H., & Makino, J. 2003, MNRAS, 340, 227, doi: [10.1046/j.1365-8711.2003.06286.x](https://doi.org/10.1046/j.1365-8711.2003.06286.x)

Belokurov, V., & Kravtsov, A. 2024, MNRAS, 528, 3198, doi: [10.1093/mnras/stad3920](https://doi.org/10.1093/mnras/stad3920)

Binney, J., & Tremaine, S. 2008, Galactic Dynamics: Second Edition

Bonaca, A., Geha, M., Küpper, A. H. W., et al. 2014, ApJ, 795, 94, doi: [10.1088/0004-637X/795/1/94](https://doi.org/10.1088/0004-637X/795/1/94)

Bonaca, A., Hogg, D. W., Price-Whelan, A. M., & Conroy, C. 2019, ApJ, 880, 38, doi: [10.3847/1538-4357/ab2873](https://doi.org/10.3847/1538-4357/ab2873)

Bonaca, A., & Price-Whelan, A. M. 2025, NewAR, 100, 101713, doi: [10.1016/j.newar.2024.101713](https://doi.org/10.1016/j.newar.2024.101713)

Bonaca, A., Naidu, R. P., Conroy, C., et al. 2021, ApJL, 909, L26, doi: [10.3847/2041-8213/abeaa9](https://doi.org/10.3847/2041-8213/abeaa9)

Bovy, J. 2015, ApJS, 216, 29, doi: [10.1088/0067-0049/216/2/29](https://doi.org/10.1088/0067-0049/216/2/29)

Bovy, J. 2026, Dynamics and Astrophysics of Galaxies (Princeton University Press)

Bovy, J., Erkal, D., & Sanders, J. L. 2017, MNRAS, 466, 628, doi: [10.1093/mnras/stw3067](https://doi.org/10.1093/mnras/stw3067)

Breivik, K., Coughlin, S., Zevin, M., et al. 2020, ApJ, 898, 71, doi: [10.3847/1538-4357/ab9d85](https://doi.org/10.3847/1538-4357/ab9d85)

Bullock, J. S., & Boylan-Kolchin, M. 2017, ARA&A, 55, 343, doi: [10.1146/annurev-astro-091916-055313](https://doi.org/10.1146/annurev-astro-091916-055313)

Bullock, J. S., & Johnston, K. V. 2005, ApJ, 635, 931, doi: [10.1086/497422](https://doi.org/10.1086/497422)

Carlberg, R. G. 2012, ApJ, 748, 20, doi: [10.1088/0004-637X/748/1/20](https://doi.org/10.1088/0004-637X/748/1/20)

—. 2025, ApJ, 989, 38, doi: [10.3847/1538-4357/adec91](https://doi.org/10.3847/1538-4357/adec91)

Chatterjee, S., Fregeau, J. M., Umbreit, S., & Rasio, F. A. 2010, ApJ, 719, 915, http://adsabs.harvard.edu/cgi-bin/nph-data_query?bibcode=2010ApJ...719..915C&link_type=EJOURNAL

Chen, C. W., & Chen, W. P. 2010, ApJ, 721, 1790, doi: [10.1088/0004-637X/721/2/1790](https://doi.org/10.1088/0004-637X/721/2/1790)

Chen, Y., & Gnedin, O. Y. 2024, The Open Journal of Astrophysics, 7, 23, doi: [10.33232/001c.116169](https://doi.org/10.33232/001c.116169)

Chen, Y., Gnedin, O. Y., & Price-Whelan, A. M. 2025a, arXiv e-prints, arXiv:2510.14924, doi: [10.48550/arXiv.2510.14924](https://doi.org/10.48550/arXiv.2510.14924)

Chen, Y., Li, H., & Gnedin, O. Y. 2025b, ApJL, 980, L18, doi: [10.3847/2041-8213/adaf93](https://doi.org/10.3847/2041-8213/adaf93)

Chen, Y., Valluri, M., Gnedin, O. Y., & Ash, N. 2025c, ApJS, 276, 32, doi: [10.3847/1538-4365/ad9904](https://doi.org/10.3847/1538-4365/ad9904)

Cloud, A., Carr, C., Tavangar, K., & Johnston, K. 2024, in American Astronomical Society Meeting Abstracts, Vol. 243, American Astronomical Society Meeting Abstracts #243, 458.24

Clutton-Brock, M. 1973, Ap&SS, 23, 55, doi: [10.1007/BF00647652](https://doi.org/10.1007/BF00647652)

Cohen, S., & Guibasm, L. 1999, in Proceedings of the Seventh IEEE International Conference on Computer Vision, Vol. 2, 1076–1083 vol.2, doi: [10.1109/ICCV.1999.790393](https://doi.org/10.1109/ICCV.1999.790393)

Cohn, H. 1980, ApJ, 242, 765, doi: [10.1086/158511](https://doi.org/10.1086/158511)

Cole, S., Lacey, C. G., Baugh, C. M., & Frenk, C. S. 2000, MNRAS, 319, 168, doi: [10.1046/j.1365-8711.2000.03879.x](https://doi.org/10.1046/j.1365-8711.2000.03879.x)

Dagum, L., & Menon, R. 1998, IEEE Computational Science and Engineering, 5, 46, doi: [10.1109/99.660313](https://doi.org/10.1109/99.660313)

Dehnen, W. 2000, ApJL, 536, L39, doi: [10.1086/312724](https://doi.org/10.1086/312724)

—. 2002, Journal of Computational Physics, 179, 27, doi: [10.1006/jcph.2002.7026](https://doi.org/10.1006/jcph.2002.7026)

Erkal, D., Belokurov, V., Bovy, J., & Sanders, J. L. 2016, MNRAS, 463, 102, doi: [10.1093/mnras/stw1957](https://doi.org/10.1093/mnras/stw1957)

Erkal, D., Belokurov, V., Laporte, C. F. P., et al. 2019, MNRAS, 487, 2685, doi: [10.1093/mnras/stz1371](https://doi.org/10.1093/mnras/stz1371)

Fardal, M. A., Huang, S., & Weinberg, M. D. 2015, MNRAS, 452, 301, doi: [10.1093/mnras/stv1198](https://doi.org/10.1093/mnras/stv1198)

Finn, D. L. 2004, MA 323 Geometric Modelling: Course Notes, Day 09 — Quintic Hermite Interpolation. <https://www.rose-hulman.edu/~finn/CCLI/Notes/day09.pdf>

Flamary, R., Courty, N., Gramfort, A., et al. 2021, Journal of Machine Learning Research, 22, 1, <http://jmlr.org/papers/v22/20-451.html>

Fouvy, J.-B., Hamilton, C., Rozier, S., & Pichon, C. 2021, MNRAS, 508, 2210, doi: [10.1093/mnras/stab2596](https://doi.org/10.1093/mnras/stab2596)

Fukushige, T., & Heggie, D. C. 2000, Monthly Notices of the Royal Astronomical Society, 318, 753, doi: [10.1046/j.1365-8711.2000.03811.x](https://doi.org/10.1046/j.1365-8711.2000.03811.x)

Gibbons, S. L. J., Belokurov, V., & Evans, N. W. 2014, MNRAS, 445, 3788, doi: [10.1093/mnras/stu1986](https://doi.org/10.1093/mnras/stu1986)

Gieles, M., Erkal, D., Antonini, F., Balbinot, E., & Peñarrubia, J. 2021, Nature Astronomy, 5, 957, doi: [10.1038/s41550-021-01392-2](https://doi.org/10.1038/s41550-021-01392-2)

Giersz, M., Heggie, D. C., & Hurley, J. R. 2008, MNRAS, 388, 429, doi: [10.1111/j.1365-2966.2008.13407.x](https://doi.org/10.1111/j.1365-2966.2008.13407.x)

Giersz, M., Heggie, D. C., Hurley, J. R., & Hypki, A. 2013, MNRAS, 431, 2184, doi: [10.1093/mnras/stt307](https://doi.org/10.1093/mnras/stt307)

Gnedin, O. Y., & Ostriker, J. P. 1997, ApJ, 474, 223, doi: [10.1086/303441](https://doi.org/10.1086/303441)

Gough, B., ed. 2009, GNU scientific library reference manual, 3rd edn. (Bristol, England: Network Theory)

Grillmair, C. J., & Dionatos, O. 2006, ApJL, 643, L17, doi: [10.1086/505111](https://doi.org/10.1086/505111)

Grondin, S. M., Webb, J. J., Lane, J. M. M., Speagle, J. S., & Leigh, N. W. C. 2024, MNRAS, 528, 5189, doi: [10.1093/mnras/stae203](https://doi.org/10.1093/mnras/stae203)

Grondin, S. M., Webb, J. J., Leigh, N. W. C., Speagle, J. S., & Khalifeh, R. J. 2022, Monthly Notices of the Royal Astronomical Society, 518, 4249, doi: [10.1093/mnras/stac3367](https://doi.org/10.1093/mnras/stac3367)

Grudić, M. Y., Hafen, Z., Rodriguez, C. L., et al. 2023, MNRAS, 519, 1366, doi: [10.1093/mnras/stac3573](https://doi.org/10.1093/mnras/stac3573)

Grudić, M. Y., & Hopkins, P. F. 2020, MNRAS, 495, 4306, doi: [10.1093/mnras/staa1453](https://doi.org/10.1093/mnras/staa1453)

Guillaume, C., Renaud, F., Martin, N. F., et al. 2026, A&A, 705, A6, doi: [10.1051/0004-6361/202557552](https://doi.org/10.1051/0004-6361/202557552)

Harris, C. R., Millman, K. J., van der Walt, S. J., et al. 2020, Nature, 585, 357, doi: [10.1038/s41586-020-2649-2](https://doi.org/10.1038/s41586-020-2649-2)

Harris, W. E. 2010, arXiv e-prints, arXiv:1012.3224. <https://arxiv.org/abs/1012.3224>

Heggie, D., & Hut, P. 2003, The Gravitational Million-Body Problem: A Multidisciplinary Approach to Star Cluster Dynamics

Hénon, M. H. 1971, Ap&SS, 14, 151, doi: [10.1007/BF00649201](https://doi.org/10.1007/BF00649201)

Hernquist, L. 1990, ApJ, 356, 359, doi: [10.1086/168845](https://doi.org/10.1086/168845)

Hernquist, L., & Ostriker, J. P. 1992, ApJ, 386, 375, doi: [10.1086/171025](https://doi.org/10.1086/171025)

Hill, D. L., & Wheeler, J. A. 1953, Physical Review, 89, 1102, doi: [10.1103/PhysRev.89.1102](https://doi.org/10.1103/PhysRev.89.1102)

Holm-Hansen, C., Chen, Y., & Gnedin, O. Y. 2025, arXiv e-prints, arXiv:2510.09604, doi: [10.48550/arXiv.2510.09604](https://doi.org/10.48550/arXiv.2510.09604)

Hunter, J. D. 2007, Computing in Science & Engineering, 9, 90, doi: [10.1109/MCSE.2007.55](https://doi.org/10.1109/MCSE.2007.55)

Ibata, R., Malhan, K., Martin, N., et al. 2021, ApJ, 914, 123, doi: [10.3847/1538-4357/abfcc2](https://doi.org/10.3847/1538-4357/abfcc2)

Ibata, R. A., Bellazzini, M., Malhan, K., Martin, N., & Bianchini, P. 2019a, Nature Astronomy, 3, 667, doi: [10.1038/s41550-019-0751-x](https://doi.org/10.1038/s41550-019-0751-x)

Ibata, R. A., Malhan, K., & Martin, N. F. 2019b, ApJ, 872, 152, doi: [10.3847/1538-4357/ab0080](https://doi.org/10.3847/1538-4357/ab0080)

Katz, H., & Ricotti, M. 2013, Monthly Notices of the Royal Astronomical Society, 432, 3250, doi: [10.1093/mnras/stt676](https://doi.org/10.1093/mnras/stt676)

King, I. R. 1966, AJ, 71, 64, doi: [10.1086/109857](https://doi.org/10.1086/109857)

Koposov, S. E., Rix, H.-W., & Hogg, D. W. 2010, ApJ, 712, 260, doi: [10.1088/0004-637X/712/1/260](https://doi.org/10.1088/0004-637X/712/1/260)

Kroupa, P. 2001, MNRAS, 322, 231, doi: [10.1046/j.1365-8711.2001.04022.x](https://doi.org/10.1046/j.1365-8711.2001.04022.x)

Kruijssen, J. M. D., Pfeffer, J. L., Chevance, M., et al. 2020, MNRAS, 498, 2472, doi: [10.1093/mnras/staa2452](https://doi.org/10.1093/mnras/staa2452)

Kullback, S., & Leibler, R. A. 1951, The Annals of Mathematical Statistics, 22, 79, doi: [10.1214/aoms/1177729694](https://doi.org/10.1214/aoms/1177729694)

Küpper, A. H. W., Kroupa, P., Baumgardt, H., & Heggie, D. C. 2010, MNRAS, 401, 105, doi: [10.1111/j.1365-2966.2009.15690.x](https://doi.org/10.1111/j.1365-2966.2009.15690.x)

Küpper, A. H. W., Lane, R. R., & Heggie, D. C. 2012, MNRAS, 420, 2700, doi: [10.1111/j.1365-2966.2011.20242.x](https://doi.org/10.1111/j.1365-2966.2011.20242.x)

Kuzma, P. B., Ishigaki, M. N., Kirihara, T., & Ogami, I. 2025, AJ, 170, 157, doi: [10.3847/1538-3881/added8e](https://doi.org/10.3847/1538-3881/added8e)

Lam, S. K., Pitrou, A., & Seibert, S. 2015, in Proc. Second Workshop on the LLVM Compiler Infrastructure in HPC, 1–6, doi: [10.1145/2833157.2833162](https://doi.org/10.1145/2833157.2833162)

Lamers, H. J. G. L. M., Baumgardt, H., & Gieles, M. 2010, Monthly Notices of the Royal Astronomical Society, 409, 305, doi: [10.1111/j.1365-2966.2010.17309.x](https://doi.org/10.1111/j.1365-2966.2010.17309.x)

Lau, C. L. 1980, Journal of the Royal Statistical Society Series C, 29, 113, doi: [10.2307/2346431](https://doi.org/10.2307/2346431)

Lowing, B., Jenkins, A., Eke, V., & Frenk, C. 2011, MNRAS, 416, 2697, doi: [10.1111/j.1365-2966.2011.19222.x](https://doi.org/10.1111/j.1365-2966.2011.19222.x)

Lynden-Bell, D., & Lynden-Bell, R. M. 1995, MNRAS, 275, 429, doi: [10.1093/mnras/275.2.429](https://doi.org/10.1093/mnras/275.2.429)

Malhan, K., & Ibata, R. A. 2019, MNRAS, 486, 2995, doi: [10.1093/mnras/stz1035](https://doi.org/10.1093/mnras/stz1035)

Malhan, K., Ibata, R. A., Carlberg, R. G., et al. 2019, ApJL, 886, L7, doi: [10.3847/2041-8213/ab530e](https://doi.org/10.3847/2041-8213/ab530e)

Malhan, K., Ibata, R. A., Sharma, S., et al. 2022, ApJ, 926, 107, doi: [10.3847/1538-4357/ac4d2a](https://doi.org/10.3847/1538-4357/ac4d2a)

Mateu, C. 2023, MNRAS, 520, 5225, doi: [10.1093/mnras/stad321](https://doi.org/10.1093/mnras/stad321)

McKinney, W. 2010, in Proceedings of the 9th Python in Science Conference, ed. S. van der Walt & J. Millman, 51 – 56

Miyamoto, M., & Nagai, R. 1975, Publ. Astron. Soc. Jap., 27, 533

Mukherjee, D., Zhu, Q., Trac, H., & Rodriguez, C. L. 2021, ApJ, 916, 9, doi: [10.3847/1538-4357/ac03b2](https://doi.org/10.3847/1538-4357/ac03b2)

Navarro, J. F., Frenk, C. S., & White, S. D. M. 1996, ApJ, 462, 563, doi: [10.1086/177173](https://doi.org/10.1086/177173)

Palau, C. G., Wang, W., & Han, J. 2025, arXiv e-prints, arXiv:2508.21408, doi: [10.48550/arXiv.2508.21408](https://doi.org/10.48550/arXiv.2508.21408)

Panithanpaisal, N., Sanderson, R. E., Rodriguez, C. L., et al. 2025, arXiv e-prints, arXiv:2509.03599, doi: [10.48550/arXiv.2509.03599](https://doi.org/10.48550/arXiv.2509.03599)

Peñarrubia, J., Benson, A. J., Martínez-Delgado, D., & Rix, H. W. 2006, *ApJ*, 645, 240, doi: [10.1086/504316](https://doi.org/10.1086/504316)

Peñarrubia, J., Walker, M. G., & Gilmore, G. 2009, *MNRAS*, 399, 1275, doi: [10.1111/j.1365-2966.2009.15027.x](https://doi.org/10.1111/j.1365-2966.2009.15027.x)

Pearson, S., Bonaca, A., Chen, Y., & Gnedin, O. Y. 2024, *ApJ*, 976, 54, doi: [10.3847/1538-4357/ad8348](https://doi.org/10.3847/1538-4357/ad8348)

Pearson, S., Price-Whelan, A. M., & Johnston, K. V. 2017, *Nature Astronomy*, 1, 633, doi: [10.1038/s41550-017-0220-3](https://doi.org/10.1038/s41550-017-0220-3)

Pfeffer, J., Kruijssen, J. M. D., Crain, R. A., & Bastian, N. 2018, *MNRAS*, 475, 4309, doi: [10.1093/mnras/stx3124](https://doi.org/10.1093/mnras/stx3124)

Piatti, A. E., & Carballo-Bello, J. A. 2020, *A&A*, 637, L2, doi: [10.1051/0004-6361/202037994](https://doi.org/10.1051/0004-6361/202037994)

Plummer, H. C. 1911, *MNRAS*, 71, 460, doi: [10.1093/mnras/71.5.460](https://doi.org/10.1093/mnras/71.5.460)

Press, W. H., Teukolsky, S. A., Vetterling, W. T., & Flannery, B. P. 2002, *Numerical recipes in C++ : the art of scientific computing*

Price-Whelan, A., Souchereau, H., Wagg, T., et al. 2024, *adrn/gala*: v1.9.1, v1.9.1, Zenodo, doi: [10.5281/zenodo.13377376](https://doi.org/10.5281/zenodo.13377376)

Rehman, S. U. 2014, *American Journal of Computational Mathematics*, 04, 446–454, doi: [10.4236/ajcm.2014.45037](https://doi.org/10.4236/ajcm.2014.45037)

Renaud, F., & Gieles, M. 2015, *MNRAS*, 448, 3416, doi: [10.1093/mnras/stv245](https://doi.org/10.1093/mnras/stv245)

Renaud, F., Gieles, M., & Boily, C. M. 2011, *MNRAS*, 418, 759, doi: [10.1111/j.1365-2966.2011.19531.x](https://doi.org/10.1111/j.1365-2966.2011.19531.x)

Riley, A. H., & Strigari, L. E. 2020, *MNRAS*, 494, 983, doi: [10.1093/mnras/staa710](https://doi.org/10.1093/mnras/staa710)

Roberts, D., Gieles, M., Erkal, D., & Sanders, J. L. 2025, *MNRAS*, 538, 454, doi: [10.1093/mnras/staf321](https://doi.org/10.1093/mnras/staf321)

Rodriguez, C. L., Hafen, Z., Grudić, M. Y., et al. 2023, *MNRAS*, 521, 124, doi: [10.1093/mnras/stad578](https://doi.org/10.1093/mnras/stad578)

Rodriguez, C. L., Morscher, M., Wang, L., et al. 2016, *MNRAS*, 463, 2109, doi: [10.1093/mnras/stw2121](https://doi.org/10.1093/mnras/stw2121)

Rodriguez, C. L., Pattabiraman, B., Chatterjee, S., et al. 2018, *Computational Astrophysics and Cosmology*, 5, 5, doi: [10.1186/s40668-018-0027-3](https://doi.org/10.1186/s40668-018-0027-3)

Rodriguez, C. L., Weatherford, N. C., Coughlin, S. C., et al. 2022, *ApJS*, 258, 22, doi: [10.3847/1538-4365/ac2edf](https://doi.org/10.3847/1538-4365/ac2edf)

Sanderson, R. E., Helmi, A., & Hogg, D. W. 2015, *ApJ*, 801, 98, doi: [10.1088/0004-637X/801/2/98](https://doi.org/10.1088/0004-637X/801/2/98)

Shea, B. L. 1988, *Journal of the Royal Statistical Society. Series C (Applied Statistics)*, 37, 466. <http://www.jstor.org/stable/2347328>

Smith, R., Flynn, C., Candlish, G. N., Fellhauer, M., & Gibson, B. K. 2015, *MNRAS*, 448, 2934, doi: [10.1093/mnras/stv228](https://doi.org/10.1093/mnras/stv228)

Sollima, A., & Mastrobuono Battisti, A. 2014, *MNRAS*, 443, 3513, doi: [10.1093/mnras/stu1426](https://doi.org/10.1093/mnras/stu1426)

Spergel, D. N., & Steinhardt, P. J. 2000, *Phys. Rev. Lett.*, 84, 3760, doi: [10.1103/PhysRevLett.84.3760](https://doi.org/10.1103/PhysRevLett.84.3760)

Spitzer, L. 1987, *Dynamical evolution of globular clusters*

Stadel, J. G. 2001, PhD thesis, University of Washington, Seattle

Stodolkiewicz, J. S. 1982, *AcA*, 32, 63

Takahashi, K., & Baumgardt, H. 2012, *MNRAS*, 420, 1799, doi: [10.1111/j.1365-2966.2011.20183.x](https://doi.org/10.1111/j.1365-2966.2011.20183.x)

Tep, K., Cook, B. T., Rodriguez, C. L., et al. 2025, *The Astrophysical Journal*, 993, 180, doi: [10.3847/1538-4357/ae0478](https://doi.org/10.3847/1538-4357/ae0478)

Thomas, G. F., Jensen, J., McConnachie, A., et al. 2020, *ApJ*, 902, 89, doi: [10.3847/1538-4357/abb6f7](https://doi.org/10.3847/1538-4357/abb6f7)

Vasiliev, E. 2015, *MNRAS*, 446, 3150, doi: [10.1093/mnras/stu2360](https://doi.org/10.1093/mnras/stu2360)

—. 2019, *MNRAS*, 482, 1525, doi: [10.1093/mnras/sty2672](https://doi.org/10.1093/mnras/sty2672)

Vasiliev, E., & Baumgardt, H. 2021, *MNRAS*, 505, 5978, doi: [10.1093/mnras/stab1475](https://doi.org/10.1093/mnras/stab1475)

Virtanen, P., Gommers, R., Oliphant, T. E., et al. 2020, *Nature Methods*, 17, 261, doi: [10.1038/s41592-019-0686-2](https://doi.org/10.1038/s41592-019-0686-2)

Wang, L., Spurzem, R., Aarseth, S., et al. 2015, *MNRAS*, 450, 4070, doi: [10.1093/mnras/stv817](https://doi.org/10.1093/mnras/stv817)

Wang, L., Spurzem, R., Aarseth, S., et al. 2016, *MNRAS*, 458, 1450, doi: [10.1093/mnras/stw274](https://doi.org/10.1093/mnras/stw274)

Weatherford, N. C., & Bonaca, A. 2025, arXiv e-prints, arXiv:2509.15307. <https://arxiv.org/abs/2509.15307>

Weatherford, N. C., Kiroğlu, F., Fragione, G., et al. 2023, *The Astrophysical Journal*, 946, 104, doi: [10.3847/1538-4357/acbcc1](https://doi.org/10.3847/1538-4357/acbcc1)

Weatherford, N. C., Rasio, F. A., Chatterjee, S., et al. 2024, *ApJ*, 967, 42, doi: [10.3847/1538-4357/ad39df](https://doi.org/10.3847/1538-4357/ad39df)

Weerasooriya, S., Starkenburg, T., Cunningham, E. C., & Johnston, K. V. 2025, arXiv e-prints, arXiv:2505.14792, doi: [10.48550/arXiv.2505.14792](https://doi.org/10.48550/arXiv.2505.14792)

Weinberg, M. D. 1996, *ApJ*, 470, 715, doi: [10.1086/177902](https://doi.org/10.1086/177902)

White, E. B., Vesperini, E., Dalessandro, E., & Varri, A. L. 2025, arXiv e-prints, arXiv:2510.15037, doi: [10.48550/arXiv.2510.15037](https://doi.org/10.48550/arXiv.2510.15037)

Yoon, J. H., Johnston, K. V., & Hogg, D. W. 2011, *ApJ*, 731, 58, doi: [10.1088/0004-637X/731/1/58](https://doi.org/10.1088/0004-637X/731/1/58)

Zhao, H. 1996, *MNRAS*, 278, 488, doi: [10.1093/mnras/278.2.488](https://doi.org/10.1093/mnras/278.2.488)

APPENDIX

A. MW POTENTIAL MODELS IN KRIOS

A.1. *Spherical Components: Galactic Bulge, Hernquist Potential, and NFW Halo*

The density of the MWPotential2014 Galactic bulge is defined in the following way¹⁰:

$$\rho(r') = \rho_0 \left(\frac{r_c}{r'} \right)^\alpha \exp \left[-(r'/r_c)^2 \right], \quad (\text{A1})$$

where we set the reference radius equal to the cutoff radius for convenience. The enclosed mass, as a function of r' , is

$$\begin{aligned} M_{\text{enc}}^{\text{Bulge}}(r') &= 4\pi \int_0^{r'} dr'' r''^2 \rho(r'') \\ &= 4\pi \rho_0 r_c^3 \int_0^{r'/r_c} du u^{-\alpha+2} \exp(-u^2). \end{aligned} \quad (\text{A2})$$

The choice of reference radius, along with the bulge mass, dictates $\rho_0 = M_b / (4\pi r_c^3 \int_0^\infty du u^{-\alpha+2} \exp(-u^2))$. This means we can write the enclosed mass as a function of M_b :

$$\begin{aligned} M_{\text{enc}}^{\text{Bulge}}(r') &= M_b \frac{\int_0^{r'/r_c} du u^{-\alpha+2} \exp(-u^2)}{\int_0^\infty du u^{-\alpha+2} \exp(-u^2)} \\ &= M_b \frac{\gamma(s, x)}{\Gamma(s)}, \end{aligned} \quad (\text{A3})$$

where $x = (r'/r_c)^2$, $s = \frac{1}{2}(3 - \alpha)$ and $\gamma(a, x)$ is the lower incomplete gamma function defined as

$$\gamma(a, x) = \int_0^x dt t^{a-1} e^{-t}. \quad (\text{A4})$$

We use the associated potential implemented in galpy and NBODY6++GPU, which reads

$$\psi_{\text{Bulge}}(r') = \frac{GM_b}{\Gamma(s)} \left(\frac{\gamma(1 - \alpha/2, x)}{r_c} - \frac{\gamma(s, x)}{r'} \right). \quad (\text{A5})$$

The bulge potential tends to a non-zero value at spatial infinity:

$$\psi_{\text{bulge}, \infty} = \frac{GM_b}{r_c} \left(\frac{\Gamma(1 - \alpha/2)}{\Gamma(s)} \right) > 0. \quad (\text{A6})$$

Therefore, if a component of this kind is included in a Galactic model (as it is in MWPotential2014), there will be bound orbits with positive energies up to $\psi_{\text{bulge}, \infty}$.

The bulge is spherically symmetric, so only $f_{v_{r'}}^{\text{Bulge}}$ is non-zero and can be computed directly from the enclosed mass:

¹⁰ <https://docs.galpy.org/en/latest/reference/potentialpowerspherwcut.html>

$$f_{v_{r'}}^{\text{Bulge}} = -\frac{GM_{\text{enc}}^{\text{Bulge}}(r')}{r'^2} = -\frac{GM_b}{r'^2} \frac{\gamma(s, x)}{\Gamma(s)}. \quad (\text{A7a})$$

The associated tidal tensor only has one non-zero term in the spherical coordinates of the host frame:

$$\partial_{r'} f_{v_{r'}}^{\text{Bulge}} = \frac{2GM_b}{r'^3} \frac{\gamma(s, x) - x^s \exp(-x)}{\Gamma(s)}. \quad (\text{A8})$$

The gravitational potential and enclosed mass for a Hernquist model (Hernquist 1990; Bovy 2026) of total mass M_H and scale radius a are

$$\psi_H(r') = -\frac{GM_H}{a} \frac{1}{(1 + r'/a)}, \quad (\text{A9a})$$

$$M_{\text{enc}, H}(r') = M_H \frac{(r'/a)^2}{(1 + r'/a)^2}, \quad (\text{A9b})$$

The spherically symmetric potential only has a non-zero gradient in the radial direction, i.e.

$$f_{v_{r'}}^H = -\frac{GM_{\text{enc}, H}(r')}{r'^2}. \quad (\text{A10})$$

For this spherically symmetric potential, we only need to compute $\partial_{r'} f_{v_{r'}}^{\text{NFW}}$ to get the tidal tensor:

$$\partial_{r'} f_{v_{r'}}^H = \frac{2GM_H}{r'^3} \frac{(r'/a)^3}{(1 + r'/a)^3}. \quad (\text{A11})$$

The NFW potential (Navarro et al. 1996; Price-Whelan et al. 2024; Bovy 2026) can be written in terms of a scale mass M_{NFW} and scale radius r_s in the following way:

$$\psi_{\text{NFW}}(r') = -\frac{GM_{\text{NFW}}}{r'} \ln \left(1 + \frac{r'}{r_s} \right). \quad (\text{A12})$$

The enclosed mass, which does not converge for NFW halos, is

$$M_{\text{enc}, \text{NFW}}(r') = M_{\text{NFW}} g(r'/r_s), \quad (\text{A13})$$

where $g(x) \equiv \ln(1 + x) - x/(1 + x)$. The associated non-zero force and tidal tensor terms (in the spherical coordinates of the host frame) are

$$f_{v_{r'}}^{\text{NFW}} = -\frac{GM_{\text{enc}, \text{NFW}}(r')}{r'^2}, \quad (\text{A14a})$$

$$\partial_{r'} f_{v_{r'}}^{\text{NFW}} = \frac{2GM_{\text{enc}, \text{NFW}}^{\text{NFW}}(r')}{r'^3} \left(1 - \frac{1}{2g(r'/r_s)} \left(\frac{r'/r_s}{1 + r'/r_s} \right)^2 \right). \quad (\text{A14b})$$

A.2. Cylindrical Components: Miyamoto-Nagai Disk

The Miyamoto-Nagai disk potential (Miyamoto & Nagai 1975; Bovy 2026) can be written in terms of the mass M_{MN} , scale length a , and scale height b :

$$\psi_{MN}(\varrho', z') = -\frac{GM_{MN}}{\sqrt{\varrho'^2 + z_{ab}^2}}, \quad (\text{A15})$$

where (ϱ', φ', z') are the cylindrical coordinates with respect to the host and $z'_{ab} \equiv \sqrt{z'^2 + b^2} + a$. The potential is axially symmetric, so we get

$$f_{v_{\varrho'}}^{MN} = -GM_{MN} \frac{\varrho'}{(\varrho'^2 + z_{ab}^2)^{3/2}}, \quad (\text{A16a})$$

$$f_{v_{\varphi'}}^{MN} = 0, \quad (\text{A16b})$$

$$f_{v_z'}^{MN} = -GM_{MN} \frac{z' z'_{ab}}{\sqrt{z'^2 + b^2} (\varrho'^2 + z_{ab}^2)^{3/2}}. \quad (\text{A16c})$$

There are four non-zero elements of the tidal tensor (in the cylindrical coordinates of the host frame) in this case:

$$\partial_{\varrho'} f_{v_{\varrho'}}^{MN} = \frac{3GM_{MN}\varrho'^2}{(\varrho'^2 + z_{ab}^2)^{5/2}} - \frac{GM_{MN}}{(\varrho'^2 + z_{ab}^2)^{3/2}}, \quad (\text{A17a})$$

$$\partial_{\varrho'} f_{v_z'}^{MN} = \partial_{z'} f_{v_{\varrho'}}^{MN} = \frac{3GM_{MN}z' \varrho' z'_{ab}}{\sqrt{z'^2 + b^2} (\varrho'^2 + z_{ab}^2)^{5/2}}, \quad (\text{A17b})$$

$$\begin{aligned} \partial_{z'} f_{v_z'}^{MN} &= \frac{3GM_{MN}z'^2 z'_{ab}}{(z'^2 + b^2)(\varrho'^2 + z_{ab}^2)^{5/2}} - \frac{GM_{MN}z'^2}{(z'^2 + b^2)(\varrho'^2 + z_{ab}^2)^{3/2}} \\ &+ \frac{GM_{MN}z'^2 z'_{ab}}{(z'^2 + b^2)^{3/2} (\varrho'^2 + z_{ab}^2)^{3/2}} - \frac{GM_{MN}z'_{ab}}{\sqrt{z'^2 + b^2} (\varrho'^2 + z_{ab}^2)^{3/2}}. \end{aligned} \quad (\text{A17c})$$

A sum of three Miyamoto-Nagai disk potentials is approximately equivalent to a double-exponential disk (Smith et al. 2015; Price-Whelan et al. 2024), with mass density $\rho(\varrho', z') \propto \exp(-\varrho'/h_{\varrho'}) \exp(-|z'|/h_z')$. This form is used in the MilkyWayPotential2022 model; see Table A.1.

A.3. MWPotential2014

A standard static model for the potential of the MW is provided in Bovy (2015), which is a sum of three potentials: a power-law density Galactic bulge that is exponentially cut off, a Miyamoto-Nagai disk, and an NFW halo. When reporting energies associated with this potential, we subtract off $\psi_{\text{bulge},\infty}$ to ensure that $\text{sgn}(E)$ remains a reliable criterion for whether a orbit is bound to the host potential.

The bulge, disk, and halo masses need to be scaled such that their contributions to the total potential are consistent with the centripetal acceleration used by NBODY6++GPU for a circular disk orbit at $r'_0 = 8 \text{ kpc}$: $f_{\text{cent}}(r'_0) = 6.32793804994 \text{ pc/Myr}^2$. The centripetal acceleration can be broken down into its the contributions from

the potential's constituent parts:

$$\begin{aligned} f_{\text{cent}}(r'_0) &= \left| f_{v_{r'}}^{\text{Bulge}}(r') + f_{v_{\varrho'}}^{\text{MN}}(\varrho' = 0, z' = 0) + f_{v_{r'}}^{\text{NFW}}(r') \right|_{r' = \varrho' = r'_0} \\ &\equiv \frac{GM_s}{r'^2}, \end{aligned} \quad (\text{A18})$$

where we use a scale mass $M_s = 9.00273072 \times 10^{10} M_{\odot}$ to ensure that each Galactic component can be scaled appropriately:

$$M_b = f_b M_s \frac{\Gamma(s)}{\gamma(s, x = (r'_0/r_c)^2)}, \quad (\text{A19a})$$

$$M_d = f_d M_s \frac{(r'^2 + (b + a)^2)^{3/2}}{r'^3}, \quad (\text{A19b})$$

$$M_h = f_h M_s \frac{1}{g(r'_0/R_s)}. \quad (\text{A19c})$$

A.4. MilkyWayPotential2022

We use a standard static model for the MW (MilkyWayPotential2022, Price-Whelan et al. 2024) with spherical and cylindrical components. The Galactic nucleus and bulge are modeled using a Hernquist potential (Hernquist 1990), the dark matter halo with an NFW potential (Navarro et al. 1996), and the disk with a sum of three Miyamoto-Nagai potentials (Miyamoto & Nagai 1975). The disk model is inspired by Smith et al. (2015), who showed that the sum of comparatively tractable terms can be used to approximate a double-exponential disk where the potential, and its associated gradients, are considerably more difficult to compute directly (Section 2.6, Binney & Tremaine 2008).

For reproducibility, we provide each orbit's initial conditions in phase space accurate to 8 decimal places in Table A.2. With these initial conditions, as well as the properties of the progenitor provided in Section 3 and host potential provided in Appendix A, KRIOS can be compared against existing particle-spray (e.g., Fardal et al. 2015; Grondin et al. 2022; Roberts et al. 2025; Chen et al. 2025c) and direct N -body models.

B. COMPARISONS TO N -BODY SIMULATIONS

B.1. Technical Details

The N -body simulations described in Section 3.1 were performed using the direct N -body code NBODY6++GPU (Wang et al. 2015), which we parametrized to include the MWPotential2014 external field. The initial conditions for the King spheres (with $W_0 = 5$) were generated from cosmic (Breivik et al. 2020). We show in Figure B.1 the typical input file of the runs made with NBODY6++GPU. Each N -body realization was composed of $N = 50000$ particles, for a total mass of $M = 10^5 M_{\odot}$, and integrated up to $t_{\text{max}} = 5 \text{ Gyr}$. We saved snapshots every $\Delta t = 1 \text{ HU}$. On a

Table A.1. The relevant physical quantities needed to recast the `MilkyWayPotential2022` model into the SCF reference frame in Hénon units. Each of the mass and scale radius values for the spherical host potential components are copied directly from the `gala` source code. The exponential disk (with scale lengths $h_{\varrho'} = 2.6$ kpc, $h_z' = 0.3$ kpc) is approximated using three Miyamoto-Nagai disks, whose properties are found using the `gala.potential.MN3ExponentialDiskPotential().get_three_potentials()` method.

Physical Quantity	Symbol	Galactic Component	Value	Units
Nucleus Mass	M_n	Galactic Nucleus (Hernquist)	1.8142×10^9	M_\odot
Scale Radius	a	Galactic Nucleus (Hernquist)	68.8867	pc
Bulge Mass	M_b	Galactic Bulge (Hernquist)	5×10^9	M_\odot
Scale Radius	a	Galactic Bulge (Hernquist)	1.0	kpc
Disk Mass	M_d	First Miyamoto-Nagai Disk	$7.872306998700792 \times 10^9$	M_\odot
Scale Length	a	First Miyamoto-Nagai Disk	1.5259431976529216	kpc
Scale Height	b	First Miyamoto-Nagai Disk	0.20663742603550295	kpc
Disk Mass	M_d	Second Miyamoto-Nagai Disk	$-2.7562522194433154 \times 10^{11}$	M_\odot
Scale Length	a	Second Miyamoto-Nagai Disk	6.782764436261113	kpc
Scale Height	b	Second Miyamoto-Nagai Disk	0.20663742603550295	kpc
Disk Mass	M_d	Third Miyamoto-Nagai Disk	$3.206184188979487 \times 10^{11}$	M_\odot
Scale Length	a	Third Miyamoto-Nagai Disk	5.894799616164217	kpc
Scale Height	b	Third Miyamoto-Nagai Disk	0.20663742603550295	kpc
Halo Scale Mass	M_h	NFW Halo	5.5427×10^{11}	M_\odot
Halo Scale Radius	r_s	NFW Halo	15.626	kpc

Table A.2. The phase-space initial conditions needed to replicate the various orbits discussed in Section 2, 3. The validation orbits use the `MWPotential2014` potential and the remaining orbits use the `MilkyWayPotential2022` potential.

Orbit ID	x_{init} [kpc]	y_{init} [kpc]	z_{init} [kpc]	$v_{x,\text{init}}$ [km/s]	$v_{y,\text{init}}$ [km/s]	$v_{z,\text{init}}$ [km/s]
Circular 0 Test	5.0	0	0	0	225.55900747	0
Circular 1 Test	20.0	0	0	0	197.61111164	0
Eccentric Test	4.04231677	0	19.58670971	0	81.49205330	0
0	-8.26114834	4.31927900	-6.25723160	-74.46836937	14.72551502	-137.10220626
1	6.65417846	-6.77625060	-6.89249860	131.88487388	-54.38017150	4.34224828
2	7.90677816	19.00502796	-7.29228303	-38.33588368	-66.85081211	111.04181836
3	9.73591969	8.80768907	0.73284850	-59.71003689	91.24008328	-39.80505238
4	-7.75511077	6.32704860	23.10803486	1.54688377	-69.83998228	18.65659155
5	-9.14496546	-2.86774379	4.55846674	25.93998870	-146.50950043	-246.21359733
6	-20.83691936	-15.77790335	-20.69545845	-13.04785291	-35.40337893	-181.82805977
7	-18.82672221	27.56963834	27.40177203	25.20438668	-112.02637209	29.55096514
8	22.45554180	35.25629955	-2.75494642	-10.73021364	-7.94047313	-128.19547342
9	-23.95107022	9.24097888	-14.06736155	27.31176344	-167.54952847	-128.11428538

40-core node with a single V100 GPU, one simulation typically required about 29 hours for the 20-kpc circular orbit, 38 hours for the eccentric orbit, and 56 hours for the 5-kpc circular orbit.

B.2. Corrections to the NBODY6++GPU Source Files

We note that a few corrections had to be made to the NBODY6++GPU source files in order to obtain an accurate

evolution of clusters subject to the `MWPotential2014` external field, which we will list now.

There is a mistake in the documentation, which instructs to provide the cluster's velocity in km/s. However, a careful study of the source files show that cluster's velocity should be given in pc/Myr instead.

The implementation of the potential and the force induced by the bulge component requires the calculation of the in-

```

1 1.0E8 5000.0 40 40 0
50000 1 1 1 400 1 1
0.02 0.01 0.10 1.0 1.0 1.0E5 2.0E-04
12.3084 2.0
0 0 1 0 1 0 2 0 0 0
0 0 0 5 0 1 0 0 0 0
2 2 0 0 0 3 0 0 0 0
0 0 0 0 0 0 0 0 0 0
0 0 0 0 0 0 0 0 0 0
1.0E-5 2E-4 0.1 1.0 1.0E-06 0.01 0.125
0.0 1.0 1.0 0 0 0.001 0 1.0
0.5 0.0 0.0 0.0
20.0 0.0 0.0 0.0 202.0992878224309 0.0

```

Figure B.1. Generic input file used for NBODY6++GPU runs. This input file sets up a simple cluster of $N=5 \cdot 10^4$ stars, initialized by a `dat.10` IC file (in Hénon units), running until $t_{\max}=5000$ Myr with outputs every 1 HU. We set the virial radius to $R_v=12.3084$ pc and the individual masses to $m=2 M_\odot$ (last two entries of the third line). In the final line, the cluster is initially placed at the position $(20.0, 0, 0)$ kpc, with initial velocity $(0, 202.0992878224309, 0)$ pc/Myr within a Galactic potential centered at $(0, 0, 0)$ and modeled by the `MWPotential2014` external potential (Bovy 2015), as given by the parameter `KZ(14)=5`. Contrary to the NBODY6++GPU documentation, the initial cluster's velocity is to be given in pc/Myr and not in km/s.

creasing incomplete gamma function, $\gamma(a, x)$, which is handled in the original code by the file `asa147.f` (Lau 1980). However, this implementation breaks down for high enough values of x (sometimes even as low as $x=4$), which almost always occurs in our runs. To remedy this issue, we replaced this file by the more recent implementation `asa239.f90` (Shea 1988) and updated the file `Makefile.in` to include this change.

We also noticed that NBODY6++GPU was using an older conversion rule between km/s and pc/Myr for the velocities in the file `mwpotinit.f`. We changed that value using the one provided by `galpy`:

$$1 \text{ km/s} = 1.022712165045695 \text{ pc/Myr.} \quad (\text{B20})$$

Finally, we modified the files `chdata.f` and `output.F` in order to save the snapshot data using `double` precision instead of `float` precision in order to be able to compute the integrals of motion with enough precision.